RSC Advances

PAPER

View Article Online
View Journal | View Issue

Check for updates

Cite this: *RSC Adv.*, 2025, **15**, 15348

A sensitive and selective electrochemical detection and kinetic analysis of methyl parathion using Au nanoparticle-decorated rGO/CuO ternary nanocomposite†

N. I. Nayem,[a] M. Sabbir Hossain,[a] Md. A. Rashed,*[a] K. M. Anis-Ul-Haque,[b] Jahir Ahmed,[cd] M. Faisal,[cd] Jari S. Algethami[cd] and Farid A. Harraz*[ce]

Received 2nd February 2025
Accepted 18th April 2025

DOI: 10.1039/d5ra00765h

rsc.li/rsc-advances

Detecting organophosphorus pesticide (OP) residues is essential for maintaining ecological integrity and monitoring public health concerns. This research developed a novel electrochemical sensor that employed composite materials based on copper oxide (CuO) nanostructures and reduced graphene oxide (rGO), customized with Au nanoparticles (AuNPs), to detect methyl parathion (MP) pesticide with high selectivity and sensitivity. The nanocomposite was synthesized in two facile steps, without the use of stabilizers or dispersants, utilizing a simple ultrasonication and photo-reduction process. Morphological analysis revealed a uniform distribution of AuNPs and rGO within the CuO nanostructure. Kinetic studies demonstrated that the electro-reduction of MP on a glassy carbon electrode (GCE) modified with Au@rGO/CuO exhibited irreversible, diffusion-controlled kinetics, with a transfer coefficient (α) value of 0.485. A sensing study employing the square wave voltammetry (SWV) technique exhibited exceptional sensitivity (3.46 μA μM^{-1} cm^{-2}), with a limit of detection (LOD) of 0.045 μM. Moreover, the Au@rGO/CuO-based sensor electrode exhibited exceptional selectivity for MP in the presence of various organic and inorganic species, along with notable reproducibility, repeatability, and stability. Overall, this electrochemical method for effective MP detection suggests that the prepared nanocomposite could contribute to the development of viable electrocatalysts.

1. Introduction

A growing population has led to the extensive use of pesticides to control insects and plant diseases, aiming to meet global food demands. However, the excessive use of pesticides may affect food quality. Overuse and misuse of pesticides can have detrimental effects on soil, water, human health, and ecological balance.[1–4] Organophosphorus pesticides (OPs), such as methyl parathion (MP), have been used in agriculture for decades, demonstrating potent effectiveness against a wide range of pests in fruit trees, cotton, rice, tea, and vegetables.[5] MP works by inhibiting acetylcholineesterase, disrupting the transmission of nerve signals in pests, which leads to paralysis and rapid death.[6,7] Consequently, even at low concentrations, MP residues are universally recognized as a significant concern. Acute poisoning from OP compounds can lead to respiratory paralysis and death.[8] Therefore, it is increasingly important for public health and environmental safety to rapidly identify and accurately quantify trace levels of OP pesticides.

Currently, several established analytical techniques are employed to detect environmental pollutants, including OP pesticides. These include gas chromatography-mass spectrometry (GC-MS),[9] high-performance liquid chromatography (HPLC),[10] liquid chromatography-mass spectrometry (LC-MS),[11] thin-layer chromatography (TLC),[12] fluorogenic and colorimetric methods,[13] and capillary electrochromatography (CEC).[14] Although these methods offer excellent precision and accuracy, they also present notable drawbacks, such as complicated pretreatment steps, high costs, the need for skilled personnel, extended detection times, poor selectivity, lack of portability, and labor-intensive procedures. In light of these challenges, considerable research efforts have focused on developing inexpensive, portable sensors for OP detection.

---

[a] Department of Chemistry, Faculty of Science, Mawlana Bhashani Science and Technology University, Santosh, Tangail, 1902, Bangladesh. E-mail: abu.rashed@mbstu.ac.bd

[b] Department of Chemistry, Jessore University of Science and Technology, Jessore, 7408, Bangladesh

[c] Advanced Materials and Nano-Research Centre (AMNRC), Najran University, Najran, 11001, Saudi Arabia. E-mail: faharraz@nu.edu.sa

[d] Department of Chemistry, Faculty of Science and Arts, Najran University, Najran, 11001, Saudi Arabia

[e] Department of Chemistry, Faculty of Science and Arts at Sharurah, Najran University, Sharurah, 68342, Saudi Arabia

† Electronic supplementary information (ESI) available. See DOI: https://doi.org/10.1039/d5ra00765h

Recently, electrochemical techniques have garnered significant interest due to their affordability, ease of use, wide detection range, outstanding sensitivity, superior selectivity, fast reaction kinetics, and minimal operating time in MP determination.[6,15] Electrochemical sensors often utilize the glassy carbon (GC) electrode as the working electrode due to its minimal reactivity, chemical resistivity, broad operating potential window, and effective conductive properties. However, the GC electrode suffers from electrode poisoning/fouling due to analyte adsorption or by-product generation, which significantly damages the electrode surface and blocks the active sites. This results in reduced repeatability and catalytic performance of the electrode.[16,17] Consequently, electrochemical measurements of biological and environmental species have increasingly focused on chemically modifying electrodes instead of relying on bare electrodes, which tend to be less effective. It is widely acknowledged that the use of functional nanomaterials for electrode modification significantly enhances the performance of electrochemical sensors.[18–20] The electrodes modified with nanomaterials facilitate electron transport by accelerating charge transfer, which ultimately improves sensitivity.[21,22] In contrast, the unmodified GC electrode exhibits a limited response to electrochemical MP detection. By tailoring the GC electrode surface with different nanomaterials, either individually or in a combination form (composite form), such as conducting polymers,[23] carbon nanomaterials,[24] and metal oxide nanostructures,[25] sensitivity for MP detection can be significantly increased. Research indicates that electrodes functionalized with nanomaterials may greatly increase the reaction rate and enhance the anti-interference capabilities of the sensor.[26,27] Moreover, it is well-documented that nanomaterials have unique electronic, optical and mechanical properties.[28] Additionally, noble metal nanoparticles, including Ag, Au, and Pt, have also attracted much interest when doping these onto a nanostructured matrix because of their remarkable conductivity and catalytic properties, which improve sensor performance.[29,30]

CuO, recognized as a P-type semiconductor, has been the subject of extensive investigation as a promising material in biosensing, which is attributed to its remarkable catalytic activity, chemical stability, and minimal overpotential for electron transport. The material exhibits a small bandgap of 1.20 eV and a nearly negligible redox potential (approximately 0.0 V *vs.* Ag/AgCl (KCl)).[31,32] However, metallic Cu nanoparticles are easily oxidized by air or dissolved oxygen, making Cu(0) less durable for electrochemical processes. As such, much research has been done on chemically stable CuO nanoparticles for various electrochemical sensor applications, including MP sensors.[25,33,34] A significant limitation of using CuO nanoparticles as efficient electrocatalysts is their propensity to agglomerate during electrode modification. Consequently, a supporting matrix is necessary to avert this aggregation.[35] As the surface-to-volume ratio decreases due to nanoparticle aggregation, the efficacy of sensing also diminishes. To address these challenges, CuO is combined with high surface area containing materials such as conducting polymers[31] and carbon nanomaterials (*e.g.*, carbon nanotube, graphene oxide, porous carbon, *etc.*) in chemical and biological sensor applications.

Recent studies highlight the frequent use of rGO in the development of electrochemical sensors, attributed to its unique catalytic properties, remarkable conductivity, outstanding mechanical strength, and significant surface-to-volume ratio.[36,37] rGO can significantly inhibit the aggregation of CuO nanostructures and increase the effective surface area of the sensor electrode. In addition, rGO is often mixed with metal oxide nanostructures and novel metal nanoparticles to produce composite materials that enhance the catalytic performance of electrochemical sensors.[38]

Among these novel metals, gold nanoparticles (AuNPs) are ideal for sensing applications because of their distinctive optical and electrical characteristics, which enhance selectivity, sensitivity, and reproducibility, ultimately boosting the sensor's performance.[39] AuNPs are doped onto a CuO/rGO composite, which has been demonstrated to be useful in sensing applications. AuNPs significantly increase both the selectivity and sensitivity of the sensor. Furthermore, AuNPs are capable of setting apart rGO sheets to inhibit aggregation *via* π–π stacking interactions, while the limited contact among the surrounding rGO segments is reduced due to its hydrophilicity.[40]

Recently, CuO nanorod[41] and CuO nanostructure anchored with conductive polymer[42] were employed to develop an electrochemical sensor platform for OP pesticide detection. Literature reveals that in the presence of OP pesticides (such as MP), CuO forms a coordination bond with the thionate or oxonate functional group,[41] which ultimately enhances the adsorption of the targeted OP pesticides onto the CuO surface. In addition, zirconia nanofiber-loaded rGO nanocomposite-modified stainless steel[43] and electrochemically reduced graphene oxide modified GCE[44] electrodes were successfully used for the lower limit detection of MP, where the RGO provides high surface area and electrical conductivity as well as high electrocatalytic performance. In addition, outstanding electrocatalytic activity of AuNPs, MIP/AuNPs/GCE,[45] and AuNPs/Nafion/GCE[46] were employed for the sensitive detection of OP pesticides (phosmet and parathion). This sensitivity could be attributed to the enlargement of the catalytic active sites and the synergistic coupling effect between AuNPs and matrix moieties, which ultimately enhanced the electron transfer between the surface of the indicator electrode and bulk (pesticide) solution.

Using the motivation of our anticipation of the positive characteristics of CuO, rGO, and AuNPs, in this study, we developed an AuNPs@rGO/CuO ternary nanocomposite in order to effectively detect and quantify MP in a neutral aqueous solution. Although the previously described MP sensor was impressive, the development of commercial sensors is hindered by high costs and intricate catalyst production processes. Therefore, we offer a simple and inexpensive method for fabricating electrocatalysts, and the current study addresses these challenges. Our demonstrated technique for catalyst fabrication is ecologically friendly because no stabilizer or dispersion was used during the nanocomposite's synthesis. Previous literature has already documented that AuNPs and CuO composite have been successfully employed for sensing applications involving methylglyoxal (MGO) and glyoxalase (GLO)[47] as well as metformin (MET).[48]

Herein, the Au@rGO/CuO ternary nanocomposite was created using a simple synthesis route involving ultrasonication followed by photo-reduction. Numerous spectroscopic and microscopic techniques were employed to thoroughly characterize the resultant Au@rGO/CuO composite. The catalytic and sensing properties of Au@rGO/CuO-modified GCEs were evaluated *via* cyclic voltammetry (CV), electrochemical impedance spectroscopy (EIS), and square wave voltammetry (SWV) methods. The sensor electrode exhibited significant selectivity despite the presence of various common interfering species. Additionally, a successful recovery experiment was conducted using the newly adjusted sensor electrode to identify MP in river water samples collected from the river banks adjacent to agricultural fields. Finally, to our knowledge, this is the first report on the fabrication of an MP sensor using the Au@rGO/CuO ternary nanocomposite materials.

2. Experimental

2.1 Materials

The materials needed to fabricate the sensor electrode CuO nanopowder (99%+ pure; APS 30–50 nm) were procured from Otto Chemie, India, and used as received. rGO, $HAuCl_4 \cdot 3H_2O$ (containing at least 49.0% of Au), and Nafion solution (5 wt%) were obtained from Sigma-Aldrich (USA). The experimental reagent for the sensors (MP) was also sourced from Sigma-Aldrich (USA). In order to make a phosphate buffer solution (PBS) with a concentration of 0.1 M, $Na_2HPO_4 \cdot 2H_2O$ and $NaH_2PO_4 \cdot 2H_2O$ salts were used. A combination of 0.1 M NaOH and 0.1 M HCl was used to regulate the pH of the buffer solution. These chemicals were used without purification after being purchased from Merck, India. The anti-interference investigation also made use of the following chemicals: K_2CO_3, $Mg(NO_3)_2$, $CaCl_2$, Na_2SO_4, KCl along with the organic species 4-NP, glucose (Glu), sucrose (Suc), chlorpyriphos (Chp) and H_2O_2, all of which were purchased and utilized in their original forms from Merck, India. The solutions used in the experiment were prepared using deionized water (DI-H_2O).

2.2 AuNPs@rGO/CuO nanocomposite fabrication

A simple ultrasonication method was employed to fabricate the reduced graphene oxide/copper oxide (rGO/CuO) nanocomposite. In this process, 470 mg CuO + 25 mg of rGO was typically sonicated continuously using an ultrasonic frequency of 40 kHz as well as ultrasonic power of 180 W for 30 minutes at room temperature in 90 mL of ethanol. To develop a 5 wt% rGO/CuO nanocomposite, the freshly prepared blend was repeatedly rinsed with a mixture of ethanol and water and then heated in an oven at 60 °C overnight. For the fabrication of the 1 wt% AuNPs@5 wt% rGO/94 wt% CuO nanocomposite, a specified mass of $HAuCl_4 \cdot 3H_2O$ salt and 1 mL of methanol was added to the as-prepared rGO/CuO nanocomposite. The mixture was then exposed to illumination for 21 hours with an Osram Hg lamp with an intensity of 2.0 mW cm^{-2} at a wavelength λ = 350 nm in a homemade closed chamber. Finally, the mixture was rinsed and dried to get the required Au@rGO/CuO electrocatalyst.

2.3 Fabricated nanocomposite characterization

The morphology and structure of the synthesized nanocomposite were methodically examined using modern microscopy and spectroscopic techniques. The structural investigation was carried out using X-ray diffraction (XRD) with Bruker D4 Endeavour utilizing Cu $K\alpha_{1/2}$ as the applied radiation source ($\lambda\alpha_1 = 154.06$ pm, $\lambda\alpha_2 = 154.44$ pm). The elemental composition and oxidation states of the components in the developed nanocomposite were investigated using X-ray photoelectron spectroscopy (XPS) using an AlKα (−10 to 1350 eV) monochromatic radiation source, Thermo Fisher, USA. Open-source XPSPEAK41 packaged software was used for XPS fine-scan peak deconvolution using a linear background with the energy calibration of C 1s at 284.5 eV. The investigation of surface morphology was carried out using techniques such as field emission scanning electron microscopy (FE-SEM), transmission electron microscopy (TEM) and high-resolution TEM (HR-TEM) technique. A scanning electron microanalyzer (JEOL-6300 F, 5 kV) connected to energy dispersive spectroscopy (EDS) was used to capture images and elemental composition. In addition, TEM and HR-TEM images were acquired using a JEOL JEM-2100F-UHF transmission electron microscope operating at an accelerating voltage of 200 kV. The microscope was equipped with a Gatan GIF 200 energy filter, and images were recorded using a 1k-CCD camera. Finally, Fourier transform infrared spectroscopy (FTIR) was conducted using Parkin-Elmer, USA, with the KBr plate method.

2.4 Assembly of the sensor electrodes and electrochemical study

The working electrode (GCE; BAS Inc. Japan) with a diameter of 3.0 mm was used for the deposition of the newly synthesized nanocomposite, which was ultimately employed as a sensor electrode for MP detection. The GCE electrode was precisely tuned before modification with the ternary Au@rGO/CuO nanocomposite. The electrode surface was rubbed using 1.0 μm diamond paste and 0.05 μm aluminum slurry and then successively washed with a water–ethanol solution to achieve a shiny surface. The electrode surface underwent modification through the established drop-cast technique. During this process, 10 mg of the nanocomposite was dissolved in 900 μL of isopropanol along with 100 μL of a 5% Nafion solution as a binder. The active catalytic layer was generated by slowly injecting 7.5 μL of the aforementioned suspension onto the surface of the electrode, using 1.5 μL of each drop, and then allowing it to dry at room temperature. The last step was to heat the Au@rGO/CuO/GC electrode for 30 min at 60 °C. Additionally, rGO/CuO/GCE and CuO/GCE electrodes were prepared for the comparative analysis with the same modification conditions. An electrochemical workstation (CHI 660E, USA) with a three-electrode system was used to investigate the electrocatalytic and sensing events. The setup included a spiral Pt, Ag/

AgCl electrode saturated with KCl, and GCE modified by ternary nanocomposite as the counter, reference, and working electrodes, respectively. Ambient conditions were maintained during the electrochemical tests.

3. Results and discussion

3.1 Physicochemical characterization of the nanocomposite

The structural characteristics of the as-synthesized nanocomposite were thoroughly examined using XRD. The usual XRD patterns for CuO, rGO/CuO, and Au@rGO/CuO are shown in Fig. 1. The CuO XRD diffraction peaks were seen at 2θ values of 32.40°, 35.48°, 38.72°, 48.60°, 53.50°, 58.17°, 61.49°, 66.23°, 67.90°, 72.43° and 75.10° corresponding to the (110), (002), (111), (112), (020), (202), (113), (310), (220), (311) and (004) planes, respectively. The acquired diffraction patterns align closely with the monoclinic crystal structure of CuO ($C2/c$ space group, JCPDS # 45-0937).[49] XRD pattern of rGO/CuO shows the diffraction peaks for CuO with an additional broad peak at peak centered $2\theta = 25.15°$ for rGO attributed to (002) crystalline plane, indicating the interlayer distance (d-spacing) of 3.53 Å.[50] However, four additional diffraction peaks were observed in the case of the ternary composite at 2θ values of 38.16°, 44.26°, 64.68° and 77.42°, which correspond to the (111), (200), (220), and (311) crystalline planes, respectively, for the cubic structure of Au according to the previously reported literature[29,51] and the standard diffraction pattern of Au (JCPDS # 04-0784).[20]

Using the Debye–Scherrer equation, the size of the CuO crystallites in both undoped CuO nanostructure and Au@rGO/CuO composite was determined.[52]

$$d = \frac{K\lambda}{\beta\cos\theta} \tag{1}$$

where the X-ray beam's wavelength (1.54 Å) is indicated by λ, the Bragg diffraction angle is θ, the full width at half maximum (FWHM) is defined by β, and the Scherrer constant in this case is K. The average crystallite size of CuO in both undoped and Au@rGO/CuO composite was calculated to be 10.99 nm and 10.19 nm, respectively, using eqn (1). This observation suggests a modest decrease in the dimensions of CuO crystallites throughout the Au photo-reduction process, which could potentially enhance the surface-to-volume ratio of the Au@rGO/CuO composite.

Further investigation into the catalyst surface composition and chemical states of AuNPs decorated rGO/CuO was carried out using XPS measurements. In Fig. S1,† the survey scan XPS spectra display Cu, O, C, and Au typical peaks at the defined binding energies (eV) with atomic % of 29.29, 44.0, 26.63, and 0.07, respectively. This finding clearly validates the successful assembly of a ternary nanocomposite. In order to examine the fine scan spectra of C, O, Cu, and Au, energy calibration was performed using a binding energy reference value of 284.5 eV for C 1s (Fig. 2(a)–(d)). As seen in Fig. 2(a), the high-resolution peak for C 1s splits into four peaks during deconvolution. The significant peak observed at the lowest binding energy of 284.5 eV is attributed to the C–C/C–H interaction.[53] The peak at 286.1 eV is indicative of C–O bonds from functional groups that contain oxygen, such as hydroxyl (–OH) and epoxy (C–O–C), in the XPS spectra addressed for reduced rGO.[54,55] Although GO is reduced to form rGO, some oxygen groups are usually retained. Meanwhile, the peaks at 287.1 eV binding energies are ascribed to C=O[56] and the peak at 288.6 eV is attributed to the O=C–O link associated with the carboxyl group.[57]

The high-resolution XPS spectra of O 1s are shown in Fig. 2(b). The presence of O^{2-} in CuO (529.8 eV) is shown by fitting the O 1s XPS spectra into distinct components,[58] whereas the peaks at 531.5 eV and 533.1 eV correspond to (O–C=O) and C–OH[59,60] in the nanocomposite, respectively.

Fig. 2(c) unveils the Cu 2p core level XPS spectrum, illustrating a binding energy separation of 20 eV between the doublet Cu $2p_{3/2}$ (934.1 eV) and Cu $2p_{1/2}$ (954.1 eV).[61] Nonetheless, a subtle positive shift in binding energies was noted concerning the prominent peaks of the reported CuO spectrum.[62] The observed shifting may occur as a result of the interaction between CuO and other precursors within the nanocomposite. Furthermore, satellite peaks were detected at elevated binding energies in comparison to the principal peaks. Two satellite peaks were observed at 940.9 eV and 943.3 eV, alongside the principal peak Cu $2p_{3/2}$ at 934.1 eV. Additionally, a satellite peak at 962.3 eV was noted for the main peak Cu $2p_{1/2}$ at 954.1 eV. These satellite peaks within the energy ranges of 940–945 eV and 960–965 eV serve as a clear indication of the CuO phase characterized by a d^9 electron configuration at the lower energy level.[63,64]

Finally, Fig. 2(d) reveals the high-resolution Au 4f spectrum, showcasing a doublet at 84.0 eV and 86.8 eV, which corresponds to Au $4f_{7/2}$ and Au $4f_{5/2}$, respectively. This outcome indicates the presence of AuNPs in their metallic form (Au^0) within the developed nanocomposite, as evidenced by the binding energies recorded at 83.9 eV and 87.6 eV.[65] Nevertheless, two shoulder-like peaks detected at binding energies of 85.2 and 88.0 eV may be linked to the cationic form of gold nanoparticles. The aforementioned results unequivocally validate

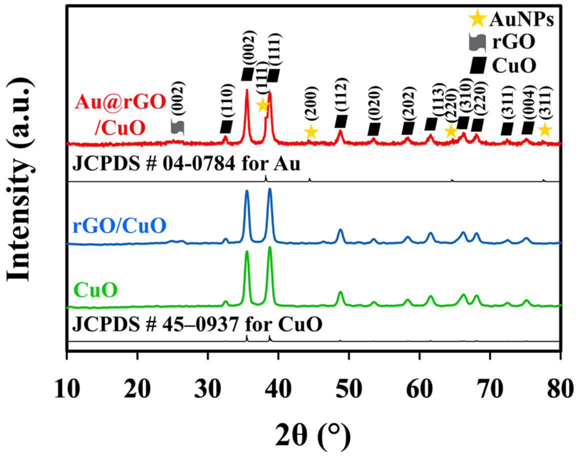

Fig. 1 Combined XRD patterns of Au@rGO/CuO, rGO/CuO, and CuO. Standard diffraction cards for Au (JCPDS # 04-0784) and CuO (JCPDS # 45-0937) are included for indexing.

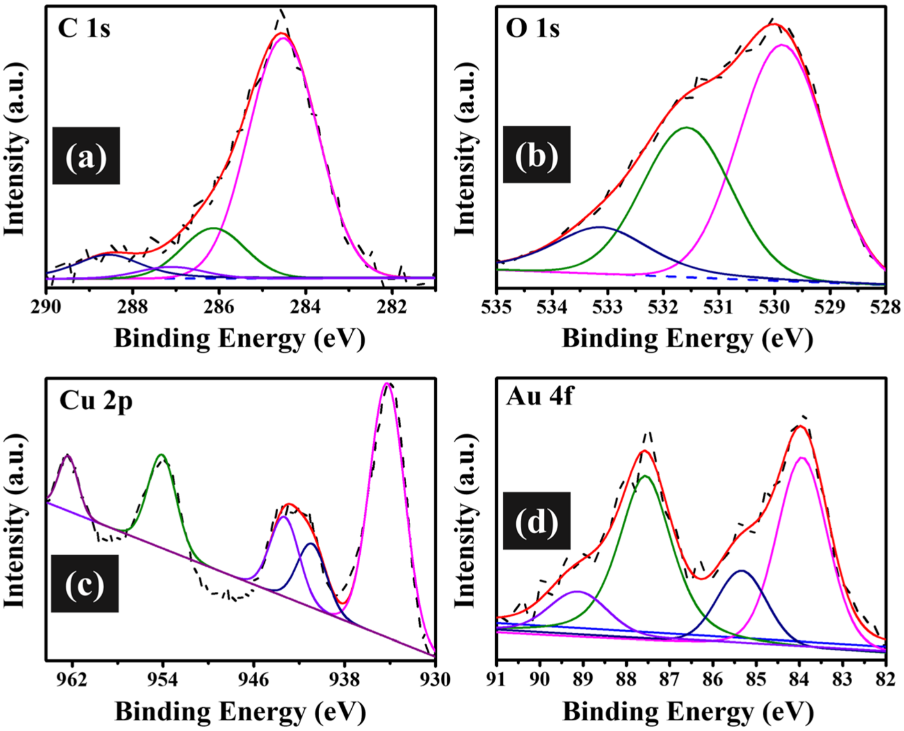

Fig. 2 XPS fine scan spectra of the Au@rGO/CuO nanocomposite: (a) C 1s, (b) O 1s, (c) Cu 2p, and (d) Au 4f.

the successful synthesis of the Au@rGO/CuO ternary nanocomposite.

The SEM technique was used to analyze the nanocomposite's morphology. Analysis of the undoped CuO and Au@rGO/CuO by SEM and EDS is shown in Fig. 3. The primary component of the nanocomposite, CuO, forms nanoflower-like structures characterized by a high surface area due to their petal-like nanosheets (Fig. 3(a)), which are advantageous for catalytic and adsorption applications. This extensive surface area also provides numerous sites for interaction with other components

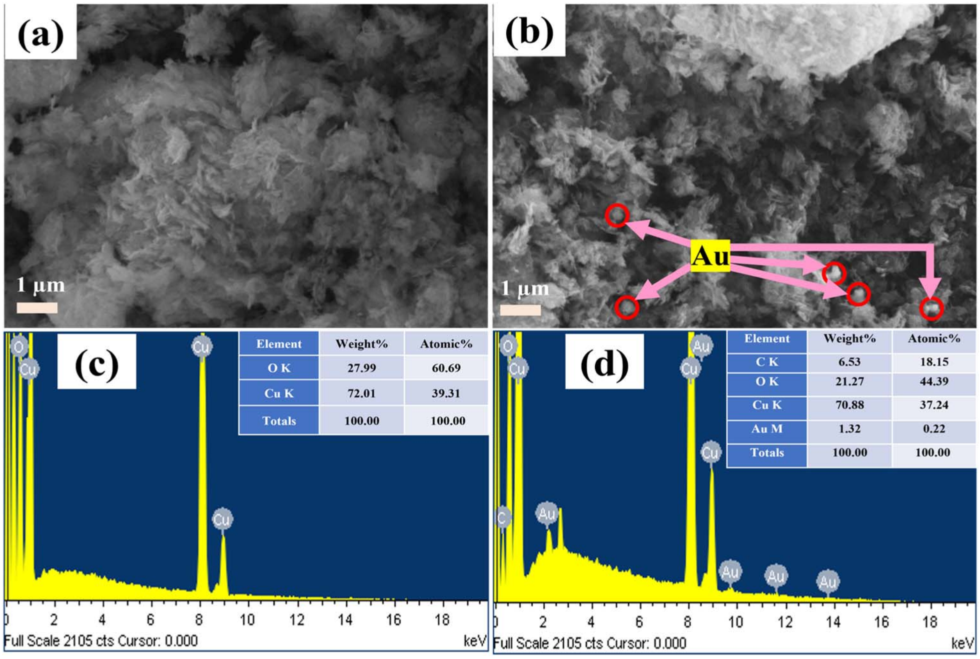

Element	Weight%	Atomic%
O K	27.99	60.69
Cu K	72.01	39.31
Totals	100.00	100.00

Element	Weight%	Atomic%
C K	6.53	18.15
O K	21.27	44.39
Cu K	70.88	37.24
Au M	1.32	0.22
Totals	100.00	100.00

Fig. 3 SEM image of CuO (a) and Au@rGO/CuO nanocomposite (b). Corresponding EDS compositional analysis for (c) CuO and (d) Au@rGO/CuO.

to enhance the composite's overall performance. In Fig. 3(b), the rGO, with its layered, wrinkled structure, acts as a conductive network within the composite, wrapping around or intercalating with the CuO nanoflowers to improve electrical conductivity. Furthermore, rGO plays a crucial role in stabilizing the dispersion of CuO nanoflowers, preventing their aggregation. Despite being present in a small quantity, the AuNPs contribute significantly due to their high catalytic activity and strong interactions with both CuO and rGO. These bright, spherical AuNPs are strategically dispersed throughout the composite, often attaching to the surfaces of CuO nanoflowers or residing within the rGO layers. The presence of AuNPs not only enhances the composite's catalytic activity but also facilitates charge transfer. The element composition of the undoped CuO and Au@rGO/CuO nanocomposite from EDS are represented in Fig. 3(c) and (d), respectively. The characteristic peaks of elements C, O, Cu, and Au certainly confirm the nanocomposite formation (Fig. 3(d)). The EDS compositional analysis (inset of Fig. 3(d)) indicates the wt% of Au is 1.32%, which is slightly higher than the theoretical 1% estimated based on the initial amount of the gold precursor ($HAuCl_4 \cdot 3H_2O$) used during the nanocomposite synthesis. This minor deviation may arise due to experimental factors such as variations in precursor deposition, the localized nature of EDS analysis, and sampling in a specific area of the nanomaterial rather than an entirely homogeneous bulk composition.

The TEM analysis in Fig. 4(a) confirms the successful integration of AuNPs within the rGO/CuO matrix, where AuNPs appear as well-dispersed high-contrast spots over the matrix surface. The high-resolution TEM (HRTEM) image in Fig. 4(b) indicates the crystalline nature of the components, with measured lattice spacings of 0.229 nm and 0.249 nm, corresponding to the (111) plane of Au and the (002) plane of CuO, respectively.[19,66] These findings indicate the presence of well-defined crystalline domains, reinforcing the structural integrity and stability of the composite. Additionally, the selected area electron diffraction (SAED) pattern in Fig. 4(c) exhibits clearly ordered centric rings, corroborating the polycrystalline nature of the as-synthesized nanocomposite. The observed lattice fringes and SAED results collectively confirm that the crystallinity of the CuO nanostructure and AuNPs are retained after the nanocomposite formation.

In the FTIR spectra of the 1% AuNPs@5% rGO/CuO nanocomposite (shown in Fig. S2†), distinct peaks were observed in comparison with those of individual rGO, CuO, and rGO/CuO samples, providing evidence of effective component integration and possible interactions. In the FTIR spectrum of rGO, bands at 1595 cm^{-1} and 3435 cm^{-1} corresponded to C═C stretching and O–H stretching, respectively. CuO displayed characteristic peaks associated with Cu–O stretching, typically appearing at 580 cm^{-1}. In the rGO/CuO composite, both CuO and rGO peaks were present with slight shifts, indicating interactions between the two components, likely through π–π stacking and metal–oxygen bonds.

Upon the addition of AuNPs to form Au@rGO/CuO, further shifts and intensity changes in the characteristic peaks of CuO and rGO were noted. These spectral modifications suggest interactions among Au, CuO, and rGO, possibly due to electron delocalization and the plasmonic effect of AuNPs. These observations support successful composite formation with synergistic properties that are appropriate for electrochemical applications. This analysis effectively showcases structural integration and component interactions crucial for sensor efficacy.

In order to investigate the chemical stability of the sensory nanomaterials, the as-fabricated ternary nanocomposite was treated with 1 M HCl and 1 M NaOH for 3 days. After 3 days, the treated nanocomposite was separated and dried completely in an oven, and the nanostructure's morphology and structural properties were characterized using the FESEM and FT-IR studies. The FESEM images after the acid-base treatment of Au@rGO/CuO showed no significant morphological changes (Fig. S3†). In the case of the FTIR study (Fig. S4†), C═C stretching and O–H stretching were observed in all cases near 1600 cm^{-1} and 3450 cm^{-1} wavenumbers, respectively. Moreover, a characteristic Cu–O stretching band was also found near 580 cm^{-1}. Other characteristic bands are in identical wavenumbers except for the changes in peak intensities.

Thus, FESEM and FTIR analyses demonstrated that Au@rGO/CuO has excellent chemical stability, as its functional groups and overall chemical structure remained intact even after exposure to harsh conditions (1 M HCl and 1 M NaOH for three days). This makes Au@rGO/CuO a robust composite

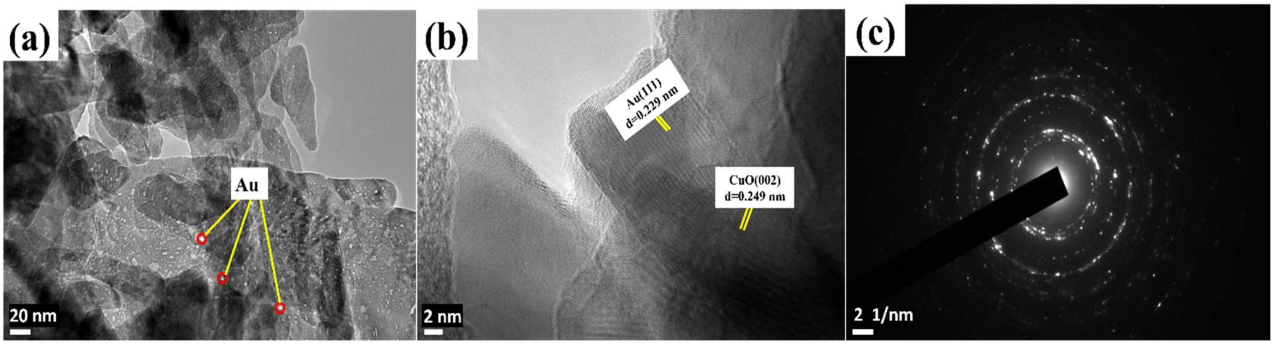

Fig. 4 TEM image of (a) the Au@rGO/CuO nanocomposite, (b) HR-TEM image of the Au@rGO/CuO nanocomposite, and (c) the SAED pattern of the Au@rGO/CuO nanocomposite.

suitable for practical applications in aqueous environmental monitoring and pollutant detection.

Moreover, the structural characterization of the sensory nanocomposite was performed using FTIR (Fig. S4†), which also revealed that the chemical structure of the desired nanocomposite remained intact after prolonged electrolysis.

3.2 Investigation of the electrochemical properties of MP on the Au@rGO/CuO/GC electrode

Fig. 5 illustrates two consecutive cycles of cyclic voltammogram observed with 30 μM MP in 0.1 M PBS (pH = 7.0) on the Au@rGO/CuO/GC electrode. During the first cathodic scan, two reduction peaks were observed at −0.042 V and −0.62 V potentials. The small peak at the (E_{pc1} −0.042 V) potential results for the reduction of Cu^+ from Cu^{2+} and the sharp irreversible reduction peak (E_{pc} −0.62 V) corresponds to the reduction of the nitro group ($-NO_2$) to hydroxylamine group (–NHOH) *via* a four-electron process (reaction (1)). This is then oxidized to the nitroso compound (–NO) during the anodic scan at (E_{pa1} −0.017 V) (reaction (2 forward)) and another small peak was observed at 0.16 V potential, addressed as Cu^+ re-oxidized to Cu^+. In the 2nd cycle, the current intensity of the reduction peak at (E_{pc1} −0.042 V) was increased compared to the 1st cycle as the nitroso group (–NO) was reversibly reduced to hydroxylamine (–NHOH) along with Cu^+ from Cu^{2+} (reaction (2 backward)), and this step is facilitated by the reduction of Cu^{2+} to Cu^+ at the same potential as well. The reversible redox peak (reaction (2)) can be ascribed to a two-electron redox process, aligning with various studies on nitroaromatic compounds.[67–69] The reduction peak (E_{pc} −0.62 V) decreased, which should be due to the minute quantity of MP present on the Au@rGO/CuO/GC electrode surface.

This result demonstrated that the Au@rGO/CuO/GCE ternary nanocomposite revealed good electroactivity toward MP. It has been reported that the noble metal Au can reduce 4-nitrophenol (4-NP) to 4-aminophenol (4-AP).[70] The irreversible reduction peak (R; $E_{pc} = -0.62$ V) resulted from the reduction of the nitro group ($-NO_2$) of MP to hydroxylamine (–NHOH) using a four-electron reduction process (reaction (1)), and the reversible redox peak O1/R1 (at E_{pa1} and E_{pc1}) having a peak splitting value of 25 mV was related to the interexchange between hydroxylamine (–NHOH) and the nitroso group (–NO) in a two-electron redox process (reaction (2)).[71] The relevant chemical reactions are shown in Scheme 1.

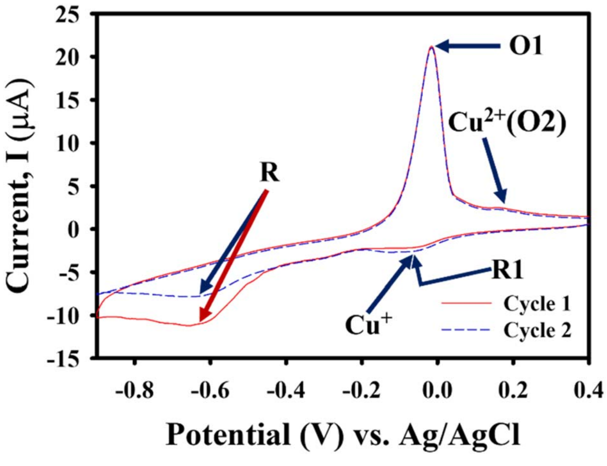

Fig. 5 Cyclic voltammograms of 2 consecutive cycles at a scan rate of 50 mV s^{-1} for 30 μm MP in 0.1 M PBS at pH = 7.0, starting from the potential of 0.4 V.

The electrocatalytic investigation of MP was performed by the CV and EIS methods (30 μM MP in 0.1 M PBS; pH = 7.0). Fig. 6(a) displays the voltammograms of both the unmodified GCE and the CuO/GCE in the presence of MP at a scan rate of 50 mV s^{-1} with a potential window ranging from +0.4 to −0.9 V. A small irreversible reduction peak ($E_{pc} = -0.73$ V) as well as oxidation peak ($E_{pa1} = 0.040$ V) were observed for the unmodified GCE. However, after modification with CuO, the irreversible reduction peak ($E_{pc} = -0.70$ V), as well as a reversible oxidation ($E_{pa1} = 0.071$ V) and reduction $E_{pc1} = 0.042$ V peaks were observed, where the potential difference for the reversible peak was estimated as $\Delta E_{(p(CuO/GCE))} = 25$ mV. As it is well documented, the catalytic ability is quantitatively enhanced when the ΔE_p value for the redox reaction decreases. CuO acts as a reducing agent towards the reduction of MP in this case. Furthermore, CuO significantly increased the intensity of current in both irreversible (R) and reversible (O1 and R1) regions, as shown in (Fig. 6(a)). This suggests that the CuO/GCE system facilitates efficient electron exchange through faradaic redox processes at the electrode/electrolyte interface. The reduction of Cu^{2+} to Cu^+ and the oxidation of Cu^+ to Cu^{2+} are the sources of the redox signal seen in CuO/GC electrodes ($E_{pc1} = -0.042$ V).[72,73]

Voltammograms using bare GCE, CuO/GCE, rGO/CuO/GCE, and Au@rGO/CuO/GCE in the presence of MP are shown in (Fig. 6(b)). The rGO/CuO/GCE and Au/rGO/CuO/GCE shows E_{pa1} (O1) as well as E_{pc1} (R1) at the same potential as CuO/GCE, but the intensity of current at E_{pa1} was higher in the case of the ternary nanocomposite rather than the binary one, where the peak E_{pa1} (O1) represents the oxidation of hydroxylamine to the nitroso group and the peak at the E_{pc1} region is attributed to the reduction of Cu^{2+} to Cu^+, combined with the reduction of the nitroso group to hydroxylamine. However, in the case of both binary and ternary composite systems, the peak potential and current intensity of E_{pa2} were the same as those of CuO/GCE. This also supports that the peak of E_{pa2} is significantly visible only for the oxidation of Cu^+ to Cu^{2+}.

In the CuO/GCE system, the cathodic irreversible peak (R) for MP electro-reduction appeared at (−0.70 V with $I_{pc} = -8.82$ μA).

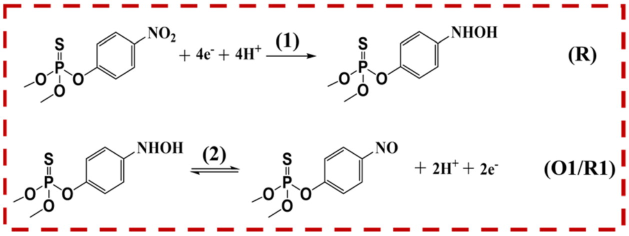

Scheme 1 Proposed electrochemical reaction mechanism.

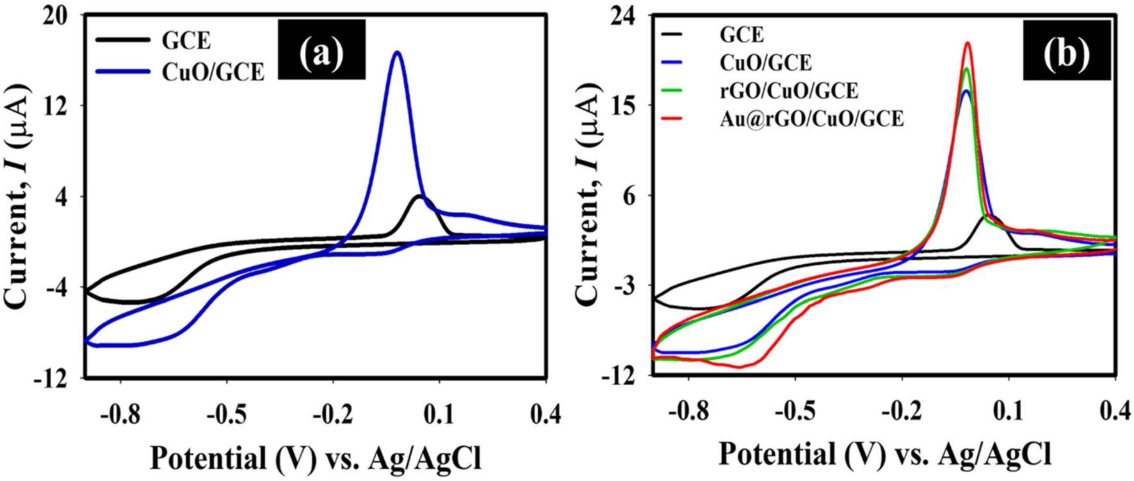

Fig. 6 Responses of CVs in the presence of 30 μm MP in 0.1 M PBS: (a) bare GCE and CuO/GCE; (b) bare GCE, CuO/GCE, rGO/CuO/GCE, and Au@rGO/CuO/GCE at a scan rate of 50 mV s^{-1}.

Furthermore, the reduction current exhibited a notable enhancement at the lower potential (−0.67 V with $I_{pc} = -9.72$ μA) when utilizing the rGO/CuO-modified GCE. Meanwhile, the Au@rGO/CuO/GC electrode exhibits a notable cathodic peak with a comparatively higher reduction current than its counterparts at a lower overpotential ($I_{pc} = -11.09$ μA, at −0.62 V). Table 1 illustrates the evaluation of the MP reductive voltammetric response, focusing on the cathodic peak current (I_{pc}) and peak potential (E_{pc}) as determined by the examined electrodes. This observation indicates that the Au@rGO/CuO/GCE exhibited superior electrocatalytic activity compared to the other electrodes assessed for MP electro-reduction.

In order to explore in detail the electrochemical properties, EIS was used to investigate the variations in charge transfer resistance (R_{ct}) among unmodified GCE, CuO/GCE, rGO/CuO/GCE, and Au@rGO/CuO/GCE.[51] Under the following conditions, −0.6 V applied potential, 1 to 10^3 Hz frequency range, and 0.05 V signal amplitude, the EIS Nyquist plot was obtained for bare GCE, CuO/GCE, rGO/CuO/GCE, and Au@rGO/CuO/GCE with respect to the MP (30 μM) test analyte in 0.1 M PBS (pH = 7.0) (Fig. S5†). The semicircle diameter of impedance spectroscopy corresponds to the interfacial electron transfer resistance (R_{ct}), which governs the electron transfer kinetics at the electrode surface.[74] The electron transfer restricted process is shown by a semicircle in the high-frequency part of the EIS Nyquist plot, while the diffusion process is shown by a straight line in the low-frequency zone.[75] Furthermore, the electrode-solution interface's lowest charge transfer resistance (R_{ct}) is indicated by the lowest semicircle diameter in the high-frequency region, which also entails the highest conductivity.[76] In this instance, a nearly straight line was seen for both unmodified GCE and CuO/GCE under the same experimental circumstances. The rGO/CuO/GCE and Au@rGO/CuO/GCE electrodes, on the other hand, exhibited a semicircle form at higher frequencies, with the Au@rGO/CuO/GCE electrode appearing to have a smaller semicircle diameter than rGO/CuO/GCE itself. Compared to the intended ternary composite modified GCE, this result shows that the unmodified GCE, CuO/GCE, and rGO/CuO/GCE electrodes produced greater R_{ct} values, *i.e.*, lower conductivity or catalytic efficiency with slow charge transfer kinetics. In conclusion, the calculated quantitative R_{ct} values for GCE, CuO/GCE, rGO/CuO/GCE, and Au@rGO/CuO/GCE were 9600 Ω, 5233 Ω, 3610 Ω, and 257 Ω, respectively. In the simulation, a simplified Randles equivalent circuit incorporating Warburg impedance (W) was used, as shown in the inset of (Fig. S5†). In comparison to GCE, CuO/GCE, and rGO/CuO/GCE, the Au@rGO/CuO nanocomposite-modified GC electrode exhibited the fastest and greatest electron transfer kinetics for MP electrochemical reduction, as confirmed by this finding.

Table 1 Analysis of the voltammetric response (specifically for peak R) in terms of peak current and peak potential during the electro-reduction of MP across various working electrodes

Electrode	E_{pc} (V)	I_{pc} (μA)
GCE	−0.73	−5.36
CuO/GCE	−0.70	−8.82
rGO/CuO/GCE	−0.67	−9.72
Au@rGO/CuO/GCE	−0.62	−11.09

The exceptional electrocatalytic performance of the developed ternary nanocomposite regarding MP can be attributed to the synergistic coupling effect and the possible enhancement of the catalytic active surface area. CuO is used in nanocomposites for electrochemical applications due to its unique properties. It is a semiconductor material with a high surface area.[77] CuO-based nanocomposites have also shown higher electrical conductivity and better catalytic performance.[78] The incorporation of rGO sheets into CuO markedly diminishes the inherent aggregation of CuO nanostructures and improves the availability of active sites on the electrode surface, facilitating electrochemical reactions. The presence of these extra active sites enhances the conductivity and catalytic performance of rGO/CuO by establishing new pathways for electron transfer. Consequently, the electrochemical performance of rGO/CuO is enhanced when compared to the pure CuO electrode material.[72] The combination of CuO and rGO results in a synergistic effect that provides rapid electron transfer kinetics, while the inclusion of AuNPs plays a crucial role owing to their outstanding catalytic properties.

In order to determine the enhancement of the active surface area, the ternary (Au@rGO/CuO) nanocomposite-modified GCE has been compared to bare GCE, and the redox probe 3.0 mM $K_3[Fe(CN)_6]$ in 0.1 M KCl was utilized. The CVs obtained using the potential scan variation approach are shown in (Fig. S6(a) and (c)†) for the GC electrode modified with Au@rGO/CuO nanocomposite and the GCE electrode alone, ranging from 5 mV s^{-1} to 100 mV s^{-1}. The Au@rGO/CuO/GCE exhibits a higher redox current when compared to the bare GCE. The cathodic and anodic peak currents for Au@rGO/CuO/GCE and bare GCE electrodes exhibit a linear relationship with the square root of the scan rate ($\nu^{1/2}$), as illustrated in (Fig. S6(b) and (d)†). The $K_3[Fe(CN)_6]^{3-/4-}$ redox system could be influenced by diffusion, as indicated by the linear relationship of the anodic peak current (I_{pa}) and cathodic peak current (I_{pc}) as a function of $\nu^{1/2}$. The next step is to determine the effective surface area (A_{eff}) of the unmodified GC electrode and the nanocomposite-modified electrode using the Randles–Sevcik equation (eqn (2)) for the reversible process.

$$I_{pa} = (2.69 \times 10^5) n^{3/2} A_{eff} D^{1/2} \nu^{1/2} C_0 \tag{2}$$

C_0 represents the concentration of the $K_3[Fe(CN)_6]^{3-/4-}$ redox probe (mol cm^{-3}). The number of electrons exchanged during the redox process is 1, while D denotes the diffusion coefficient, quantified as (7.6×10^{-6}) cm^2 s^{-1}.[79] The slope value of I_{pa} *vs.* $\nu^{1/2}$ was used to estimate the effective surface area for bare GCE as 0.45 cm^2 and for Au@rGO/CuO/GCE as 0.094 cm^2. This result indicates an increase of about 109% in the effective surface area after modifying the GCE surface with the ternary nanocomposite. However, this research found that the calculated effective surface area of the unmodified GCE (0.045 cm^2) was less than the apparent surface area (0.071 cm^2). Numerous published literature studies have also commented on the same phenomena.[18,79,80] It is crucial to highlight that we employed the Randles–Sevcik equation (eqn (2)) to assess the electroactive surface areas of the two electrodes in a precisely comparable manner, as the diffusion coefficient was maintained at a uniform value, even though the analyte's specific diffusion at each electrode is expected to vary.[18,80]

The electro-reduction performance of MP on the Au@rGO/CuO/GCE sensor electrode is influenced by the pH of the electrolyte (PBS). Fig. 7(a) shows the SWV response in the presence of 10 μM of MP with the variation of the electrolyte solution (PBS 0.1 M) pH from 5.8 to 8.8. From the voltammogram, the cathodic peak current response (Fig. 7(a)) first increased when the pH was raised from 5.8 to 7.0. After that, the SWV current response gradually decreased with increasing pH (7.0–8.8) of the solution. According to this, Au@rGO/CuO/GCE shows the highest catalytic activities in MP electro-reduction in a neutral

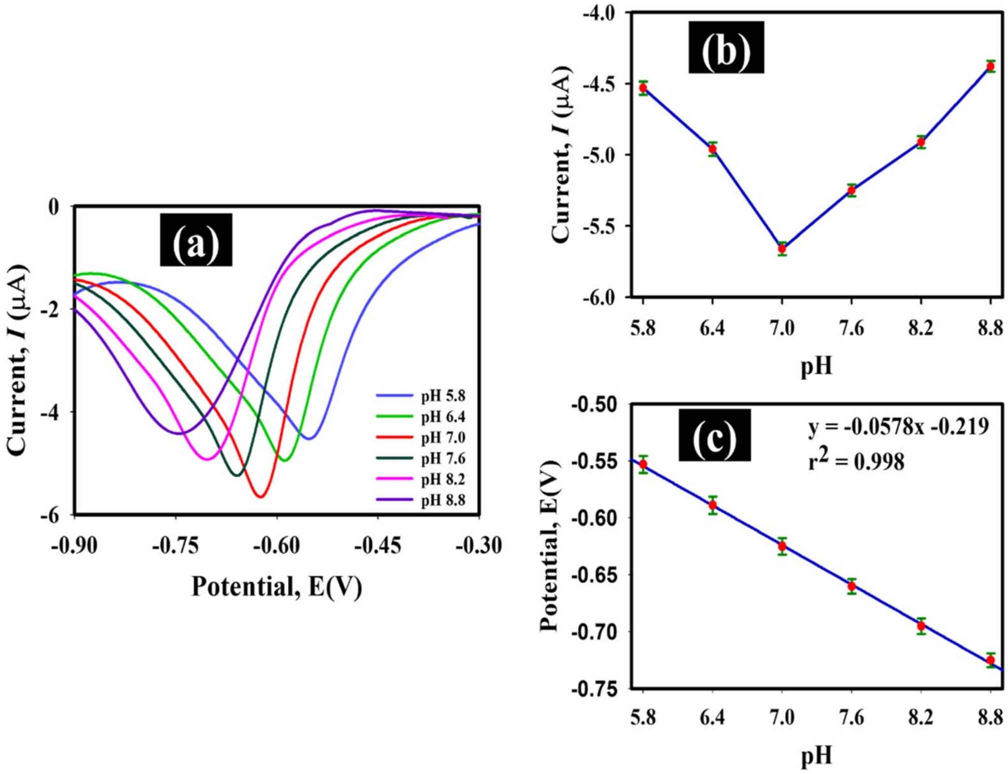

Fig. 7 (a) SWV responses of Au@rGO/CuO/GCE at various pH values (5.8–8.8) in 0.1 M PBS buffer with 10 μm MP present, within a potential window of −0.3 V to −0.9 V. (b) The reduction current intensity *vs.* electrolyte pH. (c) The peak potential fluctuation as a function of the electrolyte pH.

electrolyte condition (pH = 7.0). Because of participation in resonance, the nitrogen lone pair in the nitro group of MP's π-bonding system stays less reactive, hindering the reduction process in an acidic environment.[81] Additionally, under basic conditions, the presence of hydroxide ions at higher pH causes the hindrance of the nitro group.[81] Finally, we determined the optimal value of PBS's pH at 7.0 for further electrochemical and sensing studies of MP. Fig. 7(b) illustrates the relationship between peak current (I_p) *vs.* solution pH, with the highest current intensity observed at pH = 7.0.

The relationship between the reduction peak potential (E_p) *vs.* solution pH is depicted in Fig. 7(c). The cathodic peak exhibited a shift towards a more negative potential as the pH of the electrolyte increased. Thus, the MP electro-reduction process appears to be proton-dependent, as indicated by the straight line ($r^2 = 0.998$) with respect to the E_p *vs.* pH relationship (Fig. 7(c)). The same phenomena were observed for nitro group reduction in imidacloprid pesticide and 4-NP cases.[20,21,82] Eqn (3), which is based on the Nernst equation, illustrating the correlation between E_p and pH.

$$E_p = \frac{(-0.0592m)}{n}\text{pH} + \text{constant} \tag{3}$$

The "*m*" and "*n*" stand for the number of protons and electrons involved in the reduction process, respectively. The resulting slope value from the E_p *vs.* pH plot (Fig. 7(c)) is −0.0578 V/pH. This resulting slope value is similar to the predicted value (−0.0592 V/pH) of the Nernst equation, indicating that the quantity of protons and electrons participating in this MP electro-reduction process is equal. Scheme 1 presents the proposed mechanism for the electrochemical reduction reaction of MP on the intended Au@rGO/CuO/GCE sensor based on the literature[15,83–85] and the previously mentioned explanation.

3.3 MP reduction: a kinetics investigation

The potential scan rate variation effect provides a convenient explanation for some facts related to the electrochemical reaction process. As a result, altering the scan rate to determine the electrochemical parameters can have the following effects presumed from the link between the scan rate (ν, Vs^{-1}), peak current (I_{pc}), and peak potential (E_p) (Fig. 8(a)–(d)). By varying the scan rates from 5 mV s^{-1} to 100 mV s^{-1} in 0.1 M PBS, the electrochemical reduction of MP (30 μM) on the Au@rGO/CuO/GCE electrode was investigated (Fig. 8(a)). The irreversible electrochemical process of the MP electro-reduction (Peak "R") shows the shifting of the peak towards the negative potential direction with increasing the scan rate. A linear equation with regression value $r^2 = 0.991$, eqn (4), is obtained by plotting the cathodic peak current (I_{pc}) (for peak R) against the square root of the scan rate ($\nu^{1/2}$), which suggests that the kinetics of the MP reduction process is diffusion-controlled,[86] as shown in (Fig. 8(b)).

$$I_{pc} = 33.851\ \nu^{1/2}\left(V^{\frac{1}{2}}s^{\frac{1}{2}}\right) + 3.177;\ r^2 = 0.991 \tag{4}$$

Additionally, a projected slope value of 0.279 was derived from the plot $\log I_{pc}$ *vs.* $\log \nu$, shown in (Fig. 8(c)). The literature

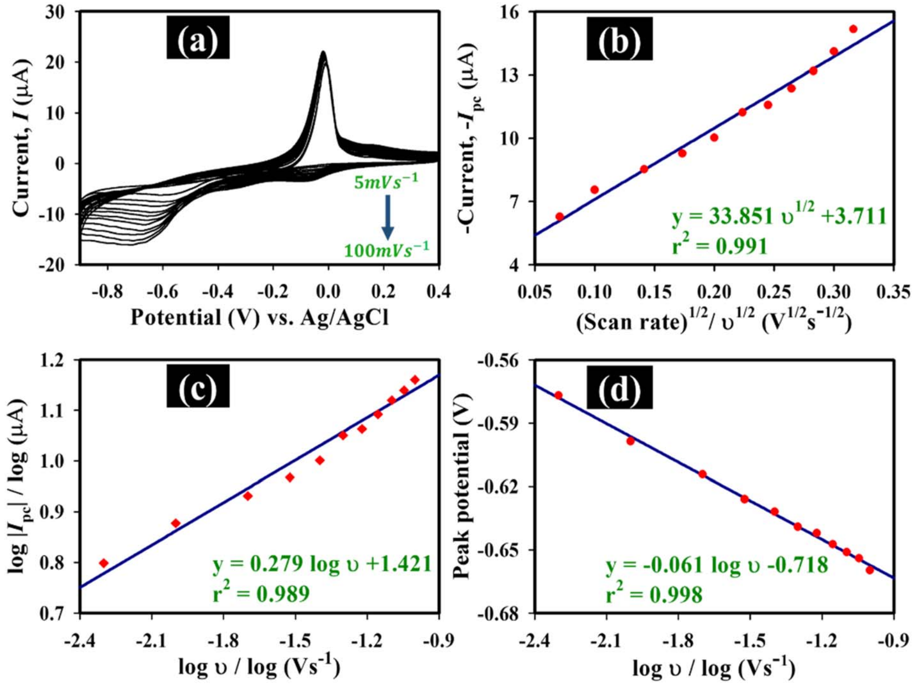

Fig. 8 (a) Voltammograms of Au@rGO/CuO/GCE at 30 μm of MP in 0.1 M PBS (pH 7.0) obtained by varying the scan rate from 5 mV s^{-1} to 100 mV^{-1}. (b) Correlation between the square root of the scan rate ($\nu^{1/2}$) and cathodic peak current (I_{pc}); (c) correlation between $\log(I_{pc})$ and log scan rate (ν); and (d) linear relationship between cathodic peak potential (E_p) and $\log \nu$.

indicates that for processes controlled solely by diffusion and those controlled entirely by adsorption, the slope values of $\log I$ against $\log \nu$ are expected to be 0.5 and 1.0, respectively.[87,88] If the slope value falls between 0.2 and 0.6, the literature states that the electrode reaction follows the diffusion-controlled process; if it falls between 0.75 and 1.0, the surface adsorption process controls the reaction kinetics; and if the value falls between 0.60 and 0.75, it is considered mixed adsorption-diffusion controlled.[89] Hence, the slope value for $\log I_{\mathrm{pc}}$ *vs.* $\log \nu$ at 0.279 indicates that the electrochemical reduction of MP at the Au@rGO/CuO/GC electrode adhered to diffusion-controlled kinetics in a neutral pH medium.

Next, from scan-rate dependent voltammograms (Fig. 8(a)), the cathodic peak potential (E_{pc}) is estimated and displayed as a function of $\log \nu$ (Fig. 8(d)), revealing a linear relationship characterized by the following regression eqn (5).

$$E_{\mathrm{pc}} = 0.061 \log \nu - 0.718\ (\nu,\ \mathrm{V\ s^{-1}},\ r^2 = 0.998) \tag{5}$$

Determining the Tafel slope (b) is crucial for evaluating the electron transfer coefficient (α) value. The Tafel slope was estimated from eqn (6) to be 122 mV dec^{-1} using the slope value of eqn (5).

$$E_{\mathrm{pc}} = \frac{(b\log\nu)}{2} + \mathrm{constant} \tag{6}$$

The literature indicates that the rate-determining steps (RDS) for the transfer of two electrons (2e$^-$) and a single electron (e$^-$) are represented by the Tafel slope values of 60 mV dec^{-1} and ≥120 mV dec^{-1}, respectively.[90] This discovery allows us to propose that the MP reduction follows a single electron (e$^-$) transfer in the RDS.

Subsequently, by applying the Tafel slope (b) value in addition to eqn (7), it is possible to estimate the electron transfer coefficient (α) for MP reduction utilizing the Au@rGO/CuO/GCE electrode.

$$b = \frac{2.303RT}{\alpha n_\alpha F} \tag{7}$$

$R = 8.314\ \mathrm{J\ K^{-1}\ mol^{-1}}$, $T = 298$ K, and $F = 96\,485\mathrm{C\ mol^{-1}}$. This equation leads to an estimate of α as 0.485, with the assumption that the electron in the rate-determining step (n_α) is 1.

3.4 Analytical performance for the detection of MP

The electrochemical sensing capabilities of the newly developed ternary nanocomposite-modified GCE were evaluated using the extremely sensitive SWV. The combination of high sensitivity and low background noise makes SWV particularly promising for electrochemical sensor study.[91] Its ability to detect trace concentrations of organic or inorganic species in complex samples and perform rapid analysis makes it a versatile and powerful technique for a wide range of electrochemical applications.

Square wave voltammetry (SWV) and differential pulse voltammetry (DPV) serve as essential techniques for electroanalysis, primarily in aqueous solvents. These methods generally exhibit sensitivity that is an order of magnitude greater than that of linear sweep voltammetry (LSV) and cyclic voltammetry (CV). For instance, SWV typically achieves detection limits in the nanomolar range, demonstrating a significant advantage over LSV. The primary concept that enhances the sensitivity of pulse techniques compared to CV/LSV lies in the varying decay rates of the faradaic and non-faradaic currents.[91] The analytical performance study depicted in Fig. 9(a) shows the SWV of the Au@rGO/CuO/GCE-based electrochemical sensor for the determination of MP at a concentration window of 0.40–39.0 μM in 0.1 M PBS (pH = 7.0) solution. The duration of accumulation frequently plays a crucial role in influencing the sensing capabilities of the developed sensor for the assessment of MP. Fig. S7† illustrates that the cathodic peak current response does not exhibit a linear relationship with the accumulation time, even as the incubation/deposition time is altered between 30 s and 180 s. However, as the deposition time varied from 120 s to 180 s, the cathodic peak current remained constant. This is because as the accumulation time was longer than 120 s, the entire effective surface area of the electrode was covered, and the peak current did not change. Therefore, a deposition time or accumulation time of 120 s was considered as optimal for SWV measurement. This result demonstrates that the optimal deposition time is essential for enhancing the determination efficiency of MP using the Au@rGO/CuO/GCE sensor. Finally, the SWV was recorded using the experimental conditions: potential window −0.3 V to −0.9 V, the pulse amplitude 0.025 V, pulse increment 0.004 V, frequency 15 Hz, and accumulation time of 120 s. It is shown that with the increase in MP concentration, the reduction peak current is upraised. Additionally, Fig. 9(b) indicates a linear relationship between the peak current and [MP], ranging from 0.40 μM to 39.0 μM. The regression equation is as follows:

$$I(\mu\mathrm{A}) = -0.325[\mathrm{MP}] - 4.174;\ (r^2 = 0.996) \tag{8}$$

The slope value, 0.325 μA μM^{-1}, is derived from eqn (8). After dividing this slope by the effective surface area of the electrode (0.094 cm^2), the sensor sensitivity was calculated, and the obtained value was 3.46 μA μM^{-1} cm^{-2}. Lastly, the following eqn (9) can be used to estimate the detection limit (LOD)[18,82] of the fabricated sensor:

$$\mathrm{LOD} = 3S_{\mathrm{b/m}}(\mathrm{S/N} = 3) \tag{9}$$

Here, S_{b} is the standard deviation of six blank (0.1 M PBS; pH = 7.0) measurements without MP, the current amounts to 0.004938 μA, and m represents the slope value calculated from Fig. 9(b). Finally, the LOD value was estimated to be 0.045 μA.

In conclusion, the newly developed electrochemical sensor has demonstrated a commendable detection limit (LOD) and detection range (LRD), coupled with rapid sensing capabilities for MP detection. Table 2 presents a comparative analysis of the developed sensor alongside previously reported relevant MP sensors, focusing on LOD and LRD.[25,34,43,44,68,69,86,92–99] The credible reason for enhancing the MP sensing performance in the

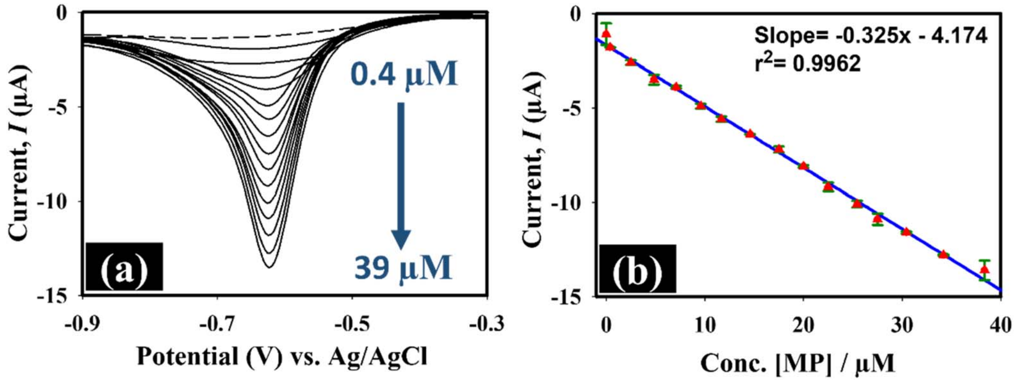

Fig. 9 (a) SWV response of Au@rGO/CuO/GCE in the potential window of −0.3 V to −0.9 V (with a 120 s accumulation time, pulse amplitude of 0.025 V, pulse increment of 0.004 V, and frequency of 15 Hz) as a function of MP concentration in 0.1 M PBS (pH = 7.0). Voltammograms without MP are displayed by the dashed line. (b) Calibration plot of reduction current *vs.* [MP].

Table 2 Analytical comparison of several electrochemical sensors for MP detection[a]

Electrode	Method	Linear range (μm)	LOD (μm)	Ref.
AuNPs-chi-GNs/GCE	SWV	0.76–3.79	0.0023	92
ERGO/GCE	SWV	0.002–0.03	0.00088	44
ERGO-CS/Hb/FTO	SWV	0.076–0.988	0.079	93
PEDOT/YSZ@rGO/SS	SWV	0.019–15.19	0.0059	43
HCP5@AuNPs-ERGO/GCE	DPV	0.005–30	0.001	86
Nafion/CuONWs-SWCNT/GCE	DPV	0.011–7.6	0.0000038	34
NanoPt-LDHs/GCE	SWV	0.001–0.0038	0.002	94
Zr/Au	SWV	0.019–0.38	0.011	95
CPE	SWV	1–60	0.05	68
Pd/MWCNTs/GCE	DPV	0.37–51.8	0.19	96
Au–TiO_2/Chit/GCE	DPV	0.0038–26.60	0.0019	97
Au/MWCNTs/GCE	DPV	1.9–60.79	0.19	98
Au/CNTs/GCE	LSV	0.5–60	0.1	99
CuO–TiO_2/GCE	DPV	0–0.0076	0.0000046	25
AuNPs/Nafion/GCE	SWV	0.5–120	0.1	69
Au@rGO/CuO/GCE	SWV	0.4–39.0	0.045	This work

[a] Chi-GNs = chi-graphene nanosheets; ERGO-CS/Hb/FTO = electrochemically reduced graphene oxide-chitosan/hemoglobin based biosensor; YSZ = yttrium-stabilized zirconia@reduced graphene oxide; HCP5@AuNPs-ERGO = hydroxylatopillar[5]arene@gold nanoparticles and electrochemical reduced graphene oxide; CuO NWs = copper oxide nanowires; NanoPt-LDHs = nanosized Pt intercalated Ni/Al layered double hydroxides.

case of the as-fabricated ternary nanocomposite is proposed as follows: (i) large surface area containing rGO hindered the aggregation of the CuO nanostructure, provides higher adsorption sites for forming coordination bonds between CuO and thionate or oxonate functional groups of MP.[41] (ii) The small-sized AuNPs nicely dispersed over the rGO/CuO surface provide high catalytic activity towards MP electroreduction with a high surface-to-volume ratio. (iii) Doping of AuNPs and rGO into CuO tailored the catalytic properties of CuO as well as led to a synergistic effect, which in turn could improve the catalytic behavior and facilitate electron transfer between Au@rGO/CuO and the MP bulk solution.

The CV response in Fig. 6(a) depicts the current response noticeably enhanced in the CuO/GCE electrode compared to bare GCE. This observation indicates that the MP sensing mechanism is dominantly governed by the semiconductor-based metal oxide (CuO). This could happen because CuO plays a critical role in preferentially binding MP molecules through the coordination interaction as well as its catalytic activity towards MP.[41] Moreover, the current response is sequentially enhanced after doping 5 wt% rGO and 1 wt% of AuNPs into the CuO nanostructure. rGO provides a high surface area, improving MP adsorption *vs.* π–π interaction, while also increasing the electrical conductivity. Finally, AuNPs catalyzed the MP electro-reduction process by significantly lowering the over-potential of 110 mV compared to bare GCE. It is well-documented that a combination of metal and metal oxide nanoparticles plays a crucial role in the electro-reduction of aromatic nitro compounds.[100] Thus, an excellent sensing performance observed for the Au@rGO/CuO/GCE sensor is likely related to the brilliant combination of the nanomaterials. CuO acts as an outstanding matrix with large surface area and adsorption sites, rGO can hinder the aggregation of the CuO nanostructure as well as facilitate the electron transport process, and homogenously dispersed minute amount of AuNPs enhance the significant catalytic performance as well as sensing. Finally, we summarize that the newly developed nanocomposite combined the advantages of different single components and therefore, exhibited new properties beyond their single constituents.[101] Furthermore, the enrichment of the adsorption-diffusion by the synergistic effect ultimately enhanced the sensing performance.

3.5 Interference, stability, and reproducibility studies

In order to ensure the validation of the suggested sensor electrode in practical applications, the selectivity test is an essential characteristic. As a result, we used the SWV approach to assess the selectivity of the as-fabricated sensor electrode in 0.1 M PBS (pH = 7.0) in the presence of a variety of typical organic and inorganic interfering species (Fig. 10). In comparison to the test analyte, MP (10 μM), five times higher concentration of interfering species were used during this selectivity study. Inorganic species, such as K_2CO_3, $Mg(NO_3)_2$, $CaCl_2$, KCl, and Na_2SO_4, along with the organic species 4-nitrophenol (4-NP), glucose (Glu), sucrose (Suc), chlorpyriphos (Chp) and H_2O_2 were chosen for the selectivity test. The anticipated sensor Au@rGO/CuO/GCE exhibited minimal to barely noticeable current response in the case of interfering species with MP. Furthermore, the same current response was obtained for MP both before and after the addition of the interfering species. The excellent selective behaviour of this sensor can be attributed to the unique molecular interactions between MP and the nanocomposite, as well as the synergistic effects of its components. MP contains a nitro ($-NO_2$) group and a phosphorus–sulfur (P=S) moiety, which play crucial roles in its electrochemical response. The aromatic nitro group undergoes a well-defined electrochemical reduction at a characteristic potential, minimizing interference from other analytes.[44,102] Additionally, the strong interaction between the P=S moiety and CuO contributes to selective adsorption and charge transfer, as copper-based nanomaterials exhibit an inherent affinity for organophosphorus compounds.[103] The Au@rGO/CuO nanocomposite further enhances this selectivity through its distinct physicochemical properties. AuNPs act as excellent electron mediators, facilitating charge transfer and catalysing the electrochemical reduction of MP.[104,105] The reduced graphene oxide (rGO) matrix provides a high surface area, improving MP adsorption *via* π–π interactions with its aromatic structure while also ensuring efficient electron transport.[106] Furthermore, the electrochemical potential of MP is distinct from those of common interfering species, enabling selective detection. The adsorption–driven interaction between MP and the Au@rGO/CuO surface leads to an enhanced electrochemical signal, differentiating it from other pesticides and common organic/inorganic interfering species. As such, these findings unequivocally demonstrate that under the given experimental circumstances, the analyzed sensor electrode exhibits good selectivity for the measurement of MP. Fig. S8(a)† shows the results of an investigation into the repeatability and stability of the anticipated sensor, which was carried out using 25 repeated CV cycles. In 0.1 M PBS, CVs were recorded at 30 μM MP with the scan rate of 50 mV s^{-1}. The variation in the intensity of the cathodic peak current as a function of the number of CV cycles is shown in Fig. S8(b).† The outcome showed that the relative standard deviation (RSD), is 1.70%. This %RSD value is exceedingly accommodating for electrochemical sensor applications. For the suggested sensor's reproducibility experiment, four GC electrodes that had been identically modified were investigated under the same experimental settings and their SWVs were recorded (Fig. S9†). According to the voltammogram responses, the peak current has a %RSD of 2.25%. Finally, the durability of the nanocomposite-modified sensor electrode during long-term storage was examined by leaving the electrode in an ambient environment for 12 days. With the exception of a slight

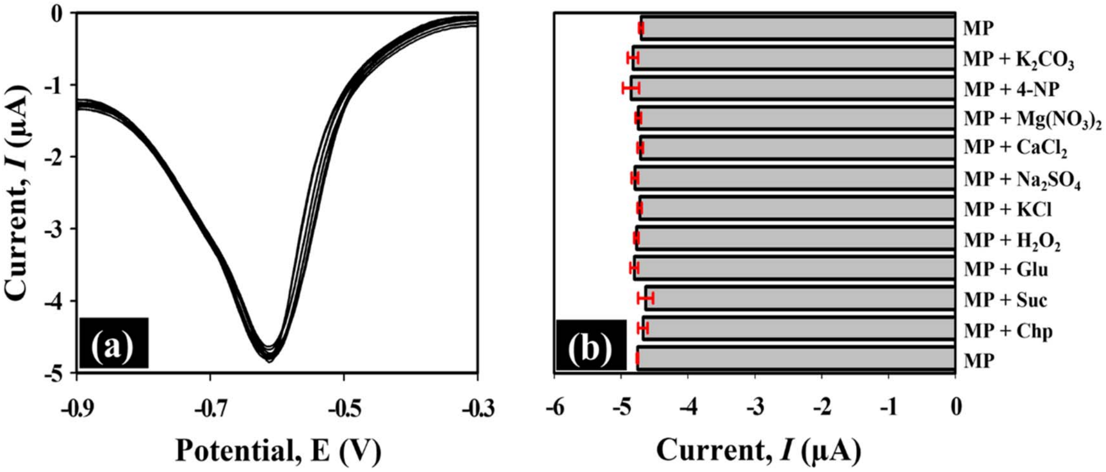

Fig. 10 (a) Selectivity test using SWV responses of Au@rGO/CuO/GCE to 10 μM MP and the concentrations of inorganic interfering species: K_2CO_3, $Mg(NO_3)_2$, $CaCl_2$, KCl, and Na_2SO_4 along with organic species: 4-NP, glucose (Glu), sucrose (Suc), chlorpyriphos (Chp), and H_2O_2 at 50 μM. (b) Bar diagram of current response *vs*. MP and above-mentioned interfering species.

decrease in current intensity from day 1 to day 12, the results showed no discernible change in peak shape (Fig. S10†). An acceptable %RSD of 3.88% was determined from four separate voltammograms by using the deviation value, as shown in the sensor analysis. It can be inferred from the above experimental results that the proposed sensor electrode has excellent sensing characteristics with respect to sensitivity, selectivity, repeatability, and storage stability.

3.6 Recovery analysis of methyl parathion in the river water sample

The developed electrochemical sensor's reliability and accuracy were carefully investigated using the conventional addition technique to recover MP from river water. The surface water was collected from the river banks adjacent to the cultivated lands (at Latitude (24.251917); Longitude (89.989555)) and (Latitude(24.162239); Longitude (89.850120)) at Bangshi and Dhaleswari rivers, respectively, in Tangail, Bangladesh. After removing all solid contaminants with filter paper ($D = 0.45$ μm), the real water samples were spiked with varying concentrations of standard MP (30, 20, and 15 μM). Each MP concentration was analyzed three times, and the average result was shown together with the standard deviation. The comprehensive experimental results are shown in Table S1.† Quantitative spiking recoveries of MP in the river water samples ranged from 96.03% to 103.88%, and the concentrations of MP found by the aforementioned approach were in agreement with the added values. This method's accuracy was further validated by the low % RSDs, which ranged from 1.31% to 3.54%. This indicates that the electrochemical sensor is highly reliable for the detection of MP in real samples.

4. Conclusion

In the present study, we focused on developing an electrochemical sensor to determine the organophosphate (OP) class MP pesticide, which is widely used in the agricultural sector. To achieve this, we used a simple and cost-effective synthesis route to fabricate an AuNPs-doped rGO/CuO ternary nanocomposite. Experiments showed that even a small amount of AuNPs might dramatically boost the catalytic activity for the electro-reduction of MP, and the newly designed nanocomposite Au@rGO/CuO showed excellent catalytic performance, probably because of the synergistic coupling effect of the components' combined catalytic properties rather than individually. Kinetic analysis showed that the electro-reduction of MP at the Au@rGO/CuO-modified GCE was an irreversible diffusion-controlled process. The sensor demonstrated a broad linear concentration range of (0.40–39.0 μM), together with a lower LOD of 0.045 μM and a high sensitivity of 3.46 $\mu A\ \mu M^{-1}\ cm^{-2}$, respectively. Additionally, during the detection of MP, the suggested sensor electrode showed a greater capacity to counteract the presence of common interfering species (both organic and inorganic). Finally, the satisfactory results of the MP recovery test conducted using surface-water samples highlight the potential benefits of using this proposed sensor electrode as an MP electrochemical sensor for real-world applications.

Data availability

The data supporting the findings of this study are available from the author upon reasonable request.

Author contributions

N. I. Nayem: conceptualization, methodology, software, formal analysis, investigation, data curation, writing – original draft. M. Sabbir Hossain: software, formal analysis, writing – original draft. Md. A. Rashed: supervision, project administration, funding acquisition, resources, validation, visualization, writing – review & editing. K. M. Anis-Ul-Haque: resources, software, data curation, writing – review & editing. Jahir Ahmed: resources, data curation, writing – review & editing. M. Faisal: data curation, formal analysis, data curation, writing – review & editing. Jari S. Algethami: resources, validation, writing – review & editing. Farid A. Harraz: project administration, validation, visualization, funding acquisition, writing – review & editing.

Conflicts of interest

The authors declare that they have no known competing financial interests or personal relationships that could have appeared to influence the work reported in this paper.

Acknowledgements

The research team thanks the Deanship of Graduate Studies and Scientific Research at Najran University for supporting the research project through the Nama'a program, with project code (NU/GP/SERC/13/425-1). The authors also acknowledge the Grants for Advanced Research in Education (GARE), Bangladesh Bureau of Educational Information & Statistics (BANBEIS) (Project ID: PS20232552), Ministry of Education, Bangladesh, for their financial assistance in this work.

References

1 A. M. Aloizou, V. Siokas, C. Vogiatzi, E. Peristeri, A. O. Docea, D. Petrakis, *et al.*, Pesticides, cognitive functions and dementia: a review, *Toxicol. Lett.*, 2020, **326**, 31–51.

2 G. K. Sidhu, S. Singh, V. Kumar, D. S. Dhanjal, S. Datta and J. Singh, Toxicity, monitoring and biodegradation of organophosphate pesticides: a review, *Crit. Rev. Environ. Sci. Technol.*, 2019, **49**(13), 1135–1187.

3 W. Mandal, S. Fajal, P. Samanta, S. Dutta, M. M. Shirolkar, Y. D. More, *et al.*, Selective and sensitive recognition of specific types of toxic organic pollutants with a chemically stable highly luminescent porous organic polymer (POP), *ACS Appl. Polym. Mater.*, 2022, **4**(11), 8633–8644.

4 S. Dutta, W. Mandal, A. V. Desai, S. Fajal, G. K. Dam, S. Mukherjee, *et al.*, A luminescent cationic MOF and its

polymer composite membrane elicit selective sensing of antibiotics and pesticides in water, *Mol. Syst. Des. Eng.*, 2023, **8**(12), 1483–1491.

5 A. Kumaravel and M. Chandrasekaran, A novel nanosilver/nafion composite electrode for electrochemical sensing of methyl parathion and parathion, *J. Electroanal. Chem.*, 2010, **638**(2), 231–235.

6 C. S. Pundir, A. Malik and Preety, Bio-sensing of organophosphorus pesticides: a review, *Biosens. Bioelectron.*, 2019, **140**, 111348.

7 J. Yuan, L. Jiang, X. Tan, Y. Yue, H. Shi and S. Feng, Fabrication of Zr(IV) modified gold electrode *via* layer-by-layer self-assembly for methyl parathion, *J. Electrochem. Soc.*, 2020, **167**(2), 027519.

8 L. G. Costa, Organophosphorus compounds at 80: some old and new issues, *Toxicol. Sci.*, 2018, **162**(1), 24–35. Available from: **https://academic.oup.com/toxsci/article/162/1/24/4706006**.

9 N. Alvarenga, W. G. Birolli, E. B. Meira, S. C. O. Lucas, I. L. de Matos, M. Nitschke, *et al.*, Biotransformation and biodegradation of methyl parathion by Brazilian bacterial strains isolated from mangrove peat, *Biocatal. Agric. Biotechnol.*, 2018, **13**, 319–326.

10 L. Chen, X. Dang, Y. Ai and H. Chen, Preparation of an acryloyl β-cyclodextrin-silica hybrid monolithic column and its application in pipette tip solid-phase extraction and HPLC analysis of methyl parathion and fenthion, *J. Sep. Sci.*, 2018, **41**(18), 3508–3514.

11 R. Moreno-González, M. E. Juan and J. M. Planas, Table olive polyphenols: a simultaneous determination by liquid chromatography–mass spectrometry, *J. Chromatogr. A*, 2020, 1609.

12 R. Akkad and W. Schwack, Determination of organophosphorus and carbamate insecticides in fresh fruits and vegetables by high-performance thin-layer chromatography-multienzyme inhibition assay, *J. AOAC Int.*, 2012, **95**(5), 1371–1377.

13 G. K. Dam, S. Fajal, S. Dutta, S. Let, A. V. Desai and S. K. Ghosh, Hydrolytically stable luminescent cationic MOF for selective detection of toxic organic arsenic in water, *ACS Appl. Opt. Mater.*, 2023, **1**(7), 1217–1226.

14 W. Wu, Y. Wu, M. Zheng, L. Yang, X. Wu, X. Lin, *et al.*, Pressurized capillary electrochromatography with indirect amperometric detection for analysis of organophosphorus pesticide residues, *Analyst*, 2010, **135**(8), 2150–2156.

15 H. Zhao, B. Liu, Y. Li, B. Li, H. Ma and S. Komarneni, One-pot green hydrothermal synthesis of bio-derived nitrogen-doped carbon sheets embedded with zirconia nanoparticles for electrochemical sensing of methyl parathion, *Ceram. Int.*, 2020, **46**(12), 19713–19722.

16 A. C. Schmidt, L. E. Dunaway, J. G. Roberts, G. S. McCarty and L. A. Sombers, Multiple scan rate voltammetry for selective quantification of real-time enkephalin dynamics, *Anal. Chem.*, 2014, **86**(15), 7806–7812.

17 M. Stoytcheva, R. Zlatev, V. Gochev, Z. Velkova, G. Montero and M. T. Beleño, Amperometric biosensors precision improvement. Application to phenolic pollutants determination, *Electrochim. Acta*, 2014, **147**, 25–30.

18 M. A. Rashed, N. Nayem, M. H. Rahman, M. Faisal, J. S. Algethami, S. Alsareii, *et al.*, A sensitive, selective non-enzymatic electrochemical detection and kinetic study of glucose over Pt nanoparticles/SWCNTs/NiO ternary nanocomposite, *J. Taiwan Inst. Chem. Eng.*, 2023, **151**, 105113.

19 M. H. Rahman, M. A. Rashed, N. I. Nayem, M. A. Rahaman, J. Ahmed, M. Faisal, *et al.*, Nanogold-decorated reduced graphene oxide/chitosan composite for electrochemical sensing of *N*-acetyl-4-aminophenol, *Mater. Chem. Phys.*, 2024, **314**, 128915.

20 F. A. Harraz, M. A. Rashed, M. Faisal, M. Alsaiari and S. A. Alsareii, Sensitive and selective electrochemical sensor for detecting 4-nitrophenole using novel gold nanoparticles/reduced graphene oxide/activated carbon nanocomposite, *Colloids Surf., A*, 2022, **654**, 130068.

21 M. A. Rashed, M. Faisal, S. A. Alsareii, M. Alsaiari, M. Jalalah and F. A. Harraz, Highly sensitive and selective electrochemical sensor for detecting imidacloprid pesticide using novel silver nanoparticles/mesoporous carbon/hematite ore ternary nanocomposite, *J. Environ. Chem. Eng.*, 2022, **10**(5), 108364.

22 M. A. Rashed, J. Ahmed, M. Faisal, S. A. Alsareii, M. Jalalah and F. A. Harraz, Highly sensitive and selective thiourea electrochemical sensor based on novel silver nanoparticles/chitosan nanocomposite, *Colloids Surf., A*, 2022, **644**, 128879.

23 F. R. Wang, G. J. Lee, N. Haridharan and J. J. Wu, Electrochemical sensor using molecular imprinting polymerization modified electrodes to detect methyl parathion in environmental media, *Electrocatalysis*, 2018, **9**(1), 1–9.

24 H. Karimi-Maleh, R. Darabi, M. Baghayeri, F. Karimi, L. Fu, J. Rouhi, *et al.*, Recent developments in carbon nanomaterials-based electrochemical sensors for methyl parathion detection, *J. Food Meas. Charact.*, 2023, **17**(5), 5371–5389.

25 X. Tian, L. Liu, Y. Li, C. Yang, Z. Zhou, Y. Nie, *et al.*, Nonenzymatic electrochemical sensor based on CuO-TiO_2 for sensitive and selective detection of methyl parathion pesticide in ground water, *Sensors Actuators, B*, 2018, **256**, 135–142.

26 K. P. Gannavarapu, V. Ganesh, M. Thakkar, S. Mitra and R. B. Dandamudi, Nanostructured diatom-ZrO_2 composite as a selective and highly sensitive enzyme free electrochemical sensor for detection of methyl parathion, *Sensors Actuators, B*, 2019, **288**, 611–617.

27 A. Othmani, *Electrodes Coated with Nanomaterials and Their Use for Environmental and Electrochemical Applications*, 2022, pp. 13–33.

28 S. Dutta, A. Sinelshchikova, J. Andreo and S. Wuttke, Nanoscience and nanotechnology for water remediation: an earnest hope toward sustainability, *Nanoscale Horiz.*, 2024, **9**(6), 885–899.

29 M. A. Rashed, F. A. Harraz, M. Faisal, A. M. El-Toni, M. Alsaiari and M. S. Al-Assiri, Gold nanoparticles plated porous silicon nanopowder for nonenzymatic voltammetric detection of hydrogen peroxide, *Anal. Biochem.*, 2021, **615**, 114065.

30 A. R. Rajamani and S. C. Peter, Novel nanostructured Pt/CeO_2@Cu_2O carbon-based electrode to magnify the electrochemical detection of the neurotransmitter dopamine and analgesic paracetamol, *ACS Appl. Nano Mater.*, 2018, **1**(9), 5148–5157.

31 M. A. Rashed, J. Ahmed, M. Faisal, S. A. Alsareii, M. Jalalah, V. Tirth, *et al.*, Surface modification of CuO nanoparticles with conducting polythiophene as a non-enzymatic amperometric sensor for sensitive and selective determination of hydrogen peroxide, *Surf. Interfaces*, 2022, **31**, 101998.

32 N. R. Dhineshbabu, V. Rajendran, N. Nithyavathy and R. Vetumperumal, Study of structural and optical properties of cupric oxide nanoparticles, *Appl. Nanosci.*, 2016, **6**(6), 933–939.

33 N. Wannasri, P. Uppachai, N. Butwong, S. Jantrasee, I. M. Isa, S. Loiha, *et al.*, A facile nonenzymatic electrochemical sensor based on copper oxide nanoparticles deposited on activated carbon for the highly sensitive detection of methyl parathion, *J. Appl. Electrochem.*, 2022, **52**(3), 595–606.

34 D. Huo, Q. Li, Y. Zhang, C. Hou and Y. Lei, A highly efficient organophosphorus pesticides sensor based on CuO nanowires-SWCNTs hybrid nanocomposite, *Sensors Actuators, B*, 2014, **199**, 410–417.

35 H. Siddiqui, M. R. Parra, P. Pandey, M. S. Qureshi and F. Z. Haque, Utility of copper oxide nanoparticles (CuO-NPs) as efficient electron donor material in bulk-heterojunction solar cells with enhanced power conversion efficiency, *J. Sci. Adv. Mater Devices*, 2020, **5**(1), 104–110.

36 Z. Wang, F. Zhang, H. Zou, Y. Yuan, H. Wang, J. Xia, *et al.*, Preparation of a Pt/NiFe layered double hydroxide/reduced graphene oxide composite as an electrocatalyst for methanol oxidation, *J. Electroanal. Chem.*, 2018, **818**, 198–203.

37 V. Mani, A. P. Periasamy and S. M. Chen, Highly selective amperometric nitrite sensor based on chemically reduced graphene oxide modified electrode, *Electrochem. Commun.*, 2012, **17**(1), 75–78.

38 N. Demir, K. Atacan, M. Ozmen and S. Z. Bas, Design of a new electrochemical sensing system based on MoS_2-TiO_2/reduced graphene oxide nanocomposite for the detection of paracetamol, *New J. Chem.*, 2020, **44**(27), 11759–11767.

39 L. Tu, Gold nanomaterials for biochemical sensing, *Gold Bull.*, 2022, **55**(2), 169–185.

40 Z. Guo, Z. Y. Wang, H. H. Wang, G. Q. Huang and M. M. Li, Electrochemical sensor for Isoniazid based on the glassy carbon electrode modified with reduced graphene oxide-Au nanomaterials, *Mater. Sci. Eng., C*, 2015, **57**, 197–204.

41 P. Sakdarat, J. Chongsuebsirikul, C. Thanachayanont, S. Prichanont and P. Pungetmongkol, Development of a nonenzymatic electrochemical sensor for organophosphate pesticide detection using copper(II) oxide nanorod electrodes, *J. Nanomater.*, 2021, **2021**, 1–11.

42 S. Sudharsan, R. Rajaram, S. Kumar, P. Swaminathan, K. Ramanujam and L. Neelakantan, Copper oxide anchored polyaniline modified glassy carbon electrode: a new sensor platform for the amperometric determination of chlorpyrifos, *Electrochim. Acta*, 2023, **471**, 143305.

43 Y. Lv, T. Yang, X. Hou, Z. Fang, K. Rajan, Y. Di, *et al.*, Zirconia nanofibers-loaded reduced graphene oxide fabrication for specific electrochemical detection of methyl parathion, *J. Alloys Compd.*, 2022, **904**, 163798.

44 T. Jeyapragasam, R. Saraswathi, S. M. Chen and B. S. Lou, Detection of methyl parathion at an electrochemically reduced graphene oxide (ERGO) modified electrode, *Int. J. Electrochem. Sci.*, 2013, **8**(11), 12353–12366.

45 Y. Zhong, Z. Li, A. Zhang, Y. Peng, H. Zhou, Y. Guo, *et al.*, Gold nanoparticle-mediated molecularly imprinted electrochemical sensor MIP/AuNPs/GCE for highly sensitive and selective detection of neutral phosmet residues in fruits and vegetables, *Microchem. J.*, 2024, **201**, 110728.

46 H. Alwael, S. H. Al-Sedran, M. Oubaha, N. A. A. Asiri, A. S. Bashammakh, A. S. Alharthy, *et al.*, Probe-integrated electrochemical sensing platform for measuring trace levels of parathion pesticides residues in water using Au-nanoparticles anchored Nafion nano composite modified glassy carbon electrode, *J. Food Compos Anal.*, 2023, **124**, 105649.

47 A. S. Rajpurohit, N. S. Punde and A. K. Srivastava, An electrochemical sensor with a copper oxide/gold nanoparticle-modified electrode for the simultaneous detection of the potential diabetic biomarkers methylglyoxal and its detoxification enzyme glyoxalase, *New J. Chem.*, 2019, **43**(42), 16572–16582.

48 M. H. Ghanbari, P. Sharafi, S. Nayebossadr and Z. Norouzi, Utilizing a nanocomposite consisting of zinc ferrite, copper oxide, and gold nanoparticles in the fabrication of a metformin electrochemical sensor supported on a glassy carbon electrode, *Microchim. Acta*, 2020, **187**(10), 557.

49 M. Ahamed, H. A. Alhadlaq, M. A. M. Khan, P. Karuppiah and N. A. Al-Dhabi, Synthesis, characterization, and antimicrobial activity of copper oxide nanoparticles, *J. Nanomater.*, 2014, **2014**, 401–409.

50 X. Jiao, Y. Qiu, L. Zhang and X. Zhang, Comparison of the characteristic properties of reduced graphene oxides synthesized from natural graphites with different graphitization degrees, *RSC Adv.*, 2017, **7**(82), 52337–52344.

51 M. A. Rashed, M. Faisal, J. Ahmed, S. A. Alsareii, M. Jalalah and F. A. Harraz, Highly sensitive and selective amperometric hydrazine sensor based on Au nanoparticle-decorated conducting polythiophene prepared *via* oxidative polymerization and photo-

reduction techniques, *J. Saudi Chem. Soc.*, 2022, **26**(3), 101480.

52 M. Faraji, Y. Yamini and N. Salehi, Characterization of magnetic nanomaterials, *Magn. Nanomater. Anal. Chem.*, 2021, 39–60.

53 M. T. Chen, Z. X. Huang, X. Ye, L. Zhang, J. J. Feng and A. J. Wang, Caffeine derived graphene-wrapped Fe3C nanoparticles entrapped in hierarchically porous Fe[sbnd] N[sbnd]C nanosheets for boosting oxygen reduction reaction, *J. Colloid Interface Sci.*, 2023, **637**, 216–224.

54 C. R. Yang, S. F. Tseng and Y. T. Chen, Characteristics of graphene oxide films reduced by using an atmospheric plasma system, *Nanomaterials*, 2018, **8**(10), 802.

55 K. Dave, K. H. Park and M. Dhayal, Two-step process for programmable removal of oxygen functionalities of graphene oxide: functional, structural and electrical characteristics, *RSC Adv.*, 2015, **5**(116), 95657–95665.

56 P. F. Li, Y. Xu and X. H. Cheng, Chemisorption of thermal reduced graphene oxide nano-layer film on TNTZ surface and its tribological behavior, *Surf. Coat. Technol.*, 2013, **232**, 331–339.

57 S. Stankovich, D. A. Dikin, R. D. Piner, K. A. Kohlhaas, A. Kleinhammes, Y. Jia, *et al.*, Synthesis of graphene-based nanosheets *via* chemical reduction of exfoliated graphite oxide, *Carbon N. Y*, 2007, **45**(7), 1558–1565.

58 W. K. Han, J. W. Choi, G. H. Hwang, S. J. Hong, J. S. Lee and S. G. Kang, Fabrication of Cu nano particles by direct electrochemical reduction from CuO nano particles, *Appl. Surf. Sci.*, 2006, **252**(8), 2832–2838.

59 Y. Wang, J. Liu, L. Liu and D. D. Sun, High-quality reduced graphene oxide-nanocrystalline platinum hybrid materials prepared by simultaneous co-reduction of graphene oxide and chloroplatinic acid, *Nanoscale Res. Lett.*, 2011, **6**(1), 241.

60 R. Al-Gaashani, A. Najjar, Y. Zakaria, S. Mansour and M. A. Atieh, XPS and structural studies of high quality graphene oxide and reduced graphene oxide prepared by different chemical oxidation methods, *Ceram. Int.*, 2019, **45**(11), 14439–14448.

61 P. Kulkarni, S. Mahamuni, M. Chandrachood, I. S. Mulla, A. P. B. Sinha, A. S. Nigavekar, *et al.*, Photoelectron spectroscopic studies on a silicon interface with Bi 2Sr2CaCu2BO8+δ high T c superconductor, *J. Appl. Phys.*, 1990, **67**(7), 3438–3442.

62 J. Yuan, J. J. Zhang, M. P. Yang, W. J. Meng, H. Wang and J. X. Lu, Cuo nanoparticles supported on TiO$_2$ with high efficiency for CO$_2$ electrochemical reduction to ethanol, *Catalysts*, 2018, **8**(4), 171.

63 K. Gupta, M. Bersani and J. A. Darr, Highly efficient electro-reduction of CO$_2$ to formic acid by nano-copper, *J. Mater. Chem. A*, 2016, **4**(36), 13786–13794.

64 P. Gao, Y. Gong, N. P. Mellott and D. Liu, Non-enzymatic amperometric detection of hydrogen peroxide using grass-like copper oxide nanostructures calcined in nitrogen atmosphere, *Electrochim. Acta*, 2015, **173**, 31–39.

65 M. Nemakal, S. Aralekallu, I. Mohammed, M. Pari, K. R. Venugopala Reddy and L. K. Sannegowda, Nanomolar detection of 4-aminophenol using amperometric sensor based on a novel phthalocyanine, *Electrochim. Acta*, 2019, **318**, 342–353.

66 B. Abebe, D. Tsegaye, C. Sori, R. C. K. Renuka Prasad and H. C. A. Murthy, Cu/CuO-Doped ZnO nanocomposites *via* solution combustion synthesis for catalytic 4-nitrophenol reduction, *ACS Omega*, 2023, **8**(10), 9597–9606.

67 D. Pan, S. Ma, X. Bo and L. Guo, Electrochemical behavior of methyl parathion and its sensitive determination at a glassy carbon electrode modified with ordered mesoporous carbon, *Microchim. Acta*, 2011, **173**(1–2), 215–221.

68 G. Liu and Y. Lin, Electrochemical stripping analysis of organophosphate pesticides and nerve agents, *Electrochem. Commun.*, 2005, **7**(4), 339–343.

69 T. F. Kang, F. Wang, L. P. Lu, Y. Zhang and T. S. Liu, Methyl parathion sensors based on gold nanoparticles and Nafion film modified glassy carbon electrodes, *Sensors Actuators, B*, 2010, **145**(1), 104–109.

70 T. Ma, W. Yang, S. Liu, H. Zhang and F. Liang, A comparison reduction of 4-nitrophenol by gold nanospheres and gold nanostars, *Catalysts*, 2017, **7**(2), 104.

71 D. Du, X. Ye, J. Zhang and D. liu, Cathodic electrochemical analysis of methyl parathion at bismuth-film-modified glassy carbon electrode, *Electrochim. Acta*, 2008, **53**(13), 4478–4484.

72 A. R. Ansari, S. A. Ansari, N. Parveen, M. O. Ansari and Z. Osman, Silver nanoparticles embedded on reduced graphene oxide@copper oxide nanocomposite for high performance supercapacitor applications, *Materials*, 2021, **14**(17), 5032.

73 W. Xu, S. Dai, G. Liu, Y. Xi, C. Hu and X. Wang, CuO Nanoflowers growing on carbon fiber fabric for flexible high-performance supercapacitors, *Electrochim. Acta*, 2016, **203**, 1–8.

74 C. Ruan, L. Yang and Y. Li, Immunobiosensor chips for detection of *Escherichia coli* O157:H7 using electrochemical impedance spectroscopy, *Anal. Chem.*, 2002, **74**(18), 4814–4820.

75 C. Erdem, D. K. Zeybek, G. Aydoğdu, B. Zeybek, Ş. Pekyardimci and E. Kiliç, Electrochemical glucose biosensor based on nickel oxide nanoparticle-modified carbon paste electrode, *Artif. Cells, Nanomed., Biotechnol.*, 2014, **42**(4), 237–244.

76 J. Hao, L. Ji, K. Wu and N. Yang, Electrochemistry of ZnO@reduced graphene oxides, *Carbon N. Y.*, 2018, **130**, 480–486.

77 J. R. Choudhuri, Metal oxide–carbon nanocomposites for electrochemical storage, *Energy, Environ. Sustainability*, 2022, 49–67.

78 D. Majumdar and S. Ghosh, Recent advancements of copper oxide based nanomaterials for supercapacitor applications, *J. Energy Storage*, 2021, **34**, 101995.

79 M. A. Rashed, M. Faisal, F. A. Harraz, M. Jalalah, M. Alsaiari and M. S. Al-Assiri, rGO/ZnO/Nafion nanocomposite as highly sensitive and selective amperometric sensor for detecting nitrite ions (NO$_2^-$), *J. Taiwan Inst. Chem. Eng.*, 2020, **112**, 345–356.

80 L. Luo, L. Zhu and Z. Wang, Nonenzymatic amperometric determination of glucose by CuO nanocubes-graphene nanocomposite modified electrode, *Bioelectrochemistry*, 2012, **88**, 156–163.

81 C. K. Chua and M. Pumera, Influence of methyl substituent position on redox properties of nitroaromatics related to 2,4,6-trinitrotoluene, *Electroanalysis*, 2011, **23**(10), 2350–2356.

82 N. Kazemifard, A. A. Ensafi and M. P. Shirani, Fabrication of a highly sensitive and selective electrochemical imidacloprid sensor using a glassy carbon electrode modified with MWCNTs/SBA-15@Si-CDs nanocomposite, *IEEE Sens. J.*, 2021, **21**(8), 9763–9770.

83 H. Zhao, H. Ma, X. Li, B. Liu, R. Liu and S. Komarneni, Nanocomposite of halloysite nanotubes/multi-walled carbon nanotubes for methyl parathion electrochemical sensor application, *Appl. Clay Sci.*, 2021, **200**, 105907.

84 R. Liu, Y. Wang, B. Li, B. Liu, H. Ma, D. Li, *et al.*, VXC-72R/ZrO2/GCE-based electrochemical sensor for the high-sensitivity detection of methyl parathion, *Materials*, 2019, **12**(21), 3637.

85 X. Yue, P. Han, W. Zhu, J. Wang and L. Zhang, Facile and sensitive electrochemical detection of methyl parathion based on a sensing platform constructed by the direct growth of carbon nanotubes on carbon paper, *RSC Adv.*, 2016, **6**(63), 58771–58779.

86 X. Hou, X. Liu, Z. Li, J. Zhang, G. Du, X. Ran, *et al.*, Electrochemical determination of methyl parathion based on pillar[5]arene@AuNPs@reduced graphene oxide hybrid nanomaterials, *New J. Chem.*, 2019, **43**(33), 13048–13057.

87 Z. Pourghobadi and R. Pourghobadi, Electrocatalytic alfuzosin oxidation on electrochemically oxidized glassy carbon modified with multiwalled carbon nanotubes and nickel oxide nanoparticles, *J. Electrochem. Soc.*, 2019, **166**(2), B76–B83.

88 P. S. Ganesh and B. E. K. Swamy, Simultaneous electroanalysis of norepinephrine, ascorbic acid and uric acid using poly(glutamic acid) modified carbon paste electrode, *J. Electroanal. Chem.*, 2015, **752**, 17–24.

89 N. Jaiswal, I. Tiwari, C. W. Foster and C. E. Banks, Highly sensitive amperometric sensing of nitrite utilizing bulk-modified MnO_2 decorated graphene oxide nanocomposite screen-printed electrodes, *Electrochim. Acta*, 2017, **227**, 255–266.

90 C. Song and J. Zhang. Electrocatalytic oxygen reduction reaction, in *PEM Fuel Cell Electrocatalysts and Catalyst Layers*, 2008, pp. 89–134.

91 A. Chen and B. Shah, Electrochemical sensing and biosensing based on square wave voltammetry, *Anal. Methods*, 2013, **5**(9), 2158–2173.

92 J. Gong, X. Miao and T. Zhou, An enzymeless organophosphate pesticide sensor using Au nanoparticle-decorated graphene hybrid nanosheet as solid-phase extraction, *Talanta*, 2011, **175**(3), 1344–1349.

93 R. Kaur, S. Rana and K. Lalit, Electrochemical detection of methyl parathion via a novel biosensor tailored on highly biocompatible electrochemically reduced graphene oxide-chitosan-hemoglobin coatings, *Biosens. Bioelectron.*, 2020, **167**, 112486.

94 J. Gong, L. Wang and X. Miao, Efficient stripping voltammetric detection of organophosphate pesticides using NanoPt intercalated Ni/Al layered double hydroxides as solid-phase extraction, *Electrochem. Commun.*, 2010, 1658–1661.

95 G. Liu and Y. Lin, Electrochemical sensor for organophosphate pesticides and nerve agents using zirconia nanoparticles as selective sorbents., *Anal. Chem.*, 2005, **77**(18), 5894–5901.

96 B. Huang, W. D. Zhang and C. H. Chen, Electrochemical determination of methyl parathion at a Pd/MWCNTs-modified electrode., *Microchim. Acta.*, 2010, **171**(1), 57–62.

97 Y. Qu, H. Min and Y. Wei, Au-TiO2/Chit modified sensor for electrochemical detection of trace organophosphates insecticides, *Talanta*, 2008, **76**(4), 758–762.

98 J. C. Ma and W. D. Zhang, Gold nanoparticle-coated multiwall carbon nanotube-modified electrode for electrochemical determination of methyl parathion, *Microchim. Acta*, 2011, **175**, 309–314.

99 Y. Zhang, T. F. Kang and Y. W. Wan, Gold nanoparticles-carbon nanotubes modified sensor for electrochemical determination of organophosphate pesticides, *Microchim Acta.*, 2009, **165**, 307–311.

100 A. Kumaravel and M. Chandrasekaran, Electrochemical determination of imidacloprid using nanosilver Nafion®/nanoTiO_2 Nafion® composite modified glassy carbon electrode, *Sensors Actuators, B*, 2011, **158**(1), 319–326.

101 S. Ivanov, U. Lange, V. Tsakova and V. M. Mirsky, Electrocatalytically active nanocomposite from palladium nanoparticles and polyaniline: oxidation of hydrazine, *Sensors Actuators, B*, 2010, **150**(1), 271–278.

102 P. Manisankar, C. Vedhi and G. Selvanathan, Electrochemical determination of methyl parathion using a modified electrode, *Toxicol. Environ. Chem.*, 2003, **85**(4–6), 233–241.

103 Y. Zhao, L. Yu, C. Song, Z. Chen, F. Meng and M. Song, Selective degradation of electron-rich organic pollutants induced by CuO@Biochar: the key role of outer-sphere interaction and singlet oxygen, *Environ. Sci. Technol.*, 2022, **56**(15), 10710–10720.

104 H. W. Chang, C. L. Chen, Y. H. Chen, Y. M. Chang, F. J. Liu and Y. C. Tsai, Electrochemical organophosphorus pesticide detection using nanostructured gold-modified electrodes, *Sensors*, 2022, **22**(24), 9938.

105 Y. Mao, H. Fa, Y. Cheng, Y. Du, W. Yin, C. Hou, *et al.*, An electrode modified with AuNPs/graphene nanocomposites film for the determination of methyl parathion residues, *Nano*, 2014, **9**(8), 1450096.

106 X. Tan, Y. Liu, T. Zhang, S. Luo, X. Liu, H. Tian, *et al.*, Ultrasensitive electrochemical detection of methyl parathion pesticide based on cationic water-soluble pillar[5]arene and reduced graphene nanocomposite, *RSC Adv.*, 2019, **9**(1), 345–353.